Article

Hydrogen-Induced Order–Disorder Effects in FePd$_3$

André Götze [1], Siobhan Christina Stevenson [2], Thomas Christian Hansen [3] and Holger Kohlmann [1],*

[1] Institute of Inorganic Chemistry, Leipzig University, Johannisallee 29, 04103 Leipzig, Germany
[2] School of Chemistry, University of Glasgow, Glasgow G12 8QQ, UK
[3] Institut Laue-Langevin, 71 Avenue des Martyrs, CS 20156, CEDEX 9, 38042 Grenoble, France
* Correspondence: holger.kohlmann@uni-leipzig.de; Tel.: +49-341-9736201

Abstract: Binary intermetallic compounds, such as FePd$_3$, attract interests due to their physical, magnetic and catalytic properties. For a better understanding of their hydrogenation properties, both ordered FePd$_3$ and disordered Fe$_{0.25}$Pd$_{0.75}$ are studied by several *in situ* methods, such as thermal analysis, X-ray powder diffraction and neutron powder diffraction, at moderate hydrogen pressures up to 8.0 MPa. FePd$_3$ absorbs small amounts of hydrogen at room temperature and follows Sieverts' law of hydrogen solubility in metals. [Pd$_6$] octahedral voids are filled up to 4.7(9)% in a statistical manner at 8.00(2) MPa, yielding the hydride FePd$_3$H$_{0.047(9)}$. This is accompanied by decreasing long-range order of Fe and Pd atoms (site occupancy factor of Fe at Wyckoff position 1a decreasing from 0.875(3) to 0.794(4)). This trend is also observed during heating, while the ordered magnetic moment decreases up to the Curie temperature of 495(8) K. The temperature dependences of the magnetic moments of iron atoms in FePd$_3$ under isobaric conditions (p(D$_2$) = 8.2(2) MPa) are consistent with a 3D Ising or Heisenberg model (critical parameter β = 0.28(5)). The atomic and magnetic order and hydrogen content of FePd$_3$ show a complex interplay.

Keywords: intermetallics; metal hydrides; neutron diffraction; in situ diffraction; order–disorder effects; interstitial hydrides; deuterides; magnetism

1. Introduction

The incorporation of hydrogen is a well-known tool for influencing the structural, electric, magnetic and optic properties of intermetallic compounds [1,2]. The interplay between hydrogen uptake and magnetism is often quite complex. Upon hydrogen uptake, intermetallic compounds may lose ferro-(LaCo$_5$) or ferrimagnetism (Y$_6$Mn$_{23}$) or become ferromagnets (CeNi$_3$, Hf$_2$Fe and Th$_7$Fe$_3$) [1]. The influence of hydrogen incorporation on the atomic order in crystal structures of intermetallics is also widely studied. In an extreme case, it may lead to amorphous hydrides in a process known as hydrogen-induced amorphization (HIA) [2]. The process involves short-range diffusion of metallic atoms, and the driving force seems to be the different hydrogen occupation sites in crystalline and amorphous states of the alloy. In some cases, such as Laves phases, the latter can be predicted by geometric factors, such as the atomic size ratio of constituting atoms [2]. Obviously, hydrogen uptake, atomic order (crystal structure) and magnetic order (cooperative phenomena) influence each other. In most studies, however, only the interaction between two of these factors is investigated and the third neglected or assumed not to play a role, which might be an oversimplification in some cases. Clearly, more in-depth investigations are needed to reveal the complex interplay between hydrogen uptake, atomic order and magnetic order in intermetallics. In this respect, we studied the crystal and magnetic structure of FePd$_3$ and its solid solution with hydrogen (also called hydride throughout this text) in detail in order to thoroughly characterize the interesting system FePd$_3$-H$_2$ and to reveal the potential cross-links between these factors. In order to obtain a high depth of knowledge, the hydrogenation of FePd$_3$ was analyzed by time-resolved *in situ*

neutron diffraction, mapping the crystal structure, including hydrogen atom positions and magnetic moments.

$FePd_3$ has attracted interest as a functional material due to its diverse physical properties. It has a characteristic pressure-induced invar behavior by means of an anomalously low thermal expansion at high applied pressures [3–5], and it is ferromagnetic with a Curie temperature of 499 K [6]. A soft ferromagnetic behavior was found in carbon-based materials by encapsulation of $FePd_3$ [7–9]. $FePd_3$ can be used in electrocatalysis to enhance the cycle stability of hybrid Li–air batteries [10] or as an electrocatalyst to oxidize formic acid [11]. In addition, a higher attraction between 2-methylfuran and hydrogen compared to palladium was found in hydrogenation catalysis [12]. The use of bimetallic catalysts changes the electronic structure at the surface [13] and decreases the Pd-Pd coordination number; this can hinder the formation of unfavorable surface species, thus avoiding unwanted side reactions, e.g., decarbonylation, in the solvent-free hydrodeoxygenation of furan compounds for a $Pd-FeO_x/SiO_2$ catalyst [14]. Knowledge of the crystal structure is of great importance for catalytic applications, since it has a distinct influence on catalytic properties. The phase diagram of the Fe-Pd system shows a solid solution with a large phase width of about $\pm 10\%$ around an Fe:Pd atomic ratio of 1:3 [15]. In addition to the disordered phase $Fe_{0.25}Pd_{0.75}$ (Cu type, $Fm\bar{3}m$), an ordered phase is known. $FePd_3$ crystallizes in an ordered variant of a cubic close packing ($AuCu_3$ type, $Pm\bar{3}m$, Figure 1). The annealing times for the ordering process are long due to similar electronic and geometric properties of the constituting atoms [16]. $FePd_3$, with a high degree of crystallographic order, shows a higher hydrogen incorporation at high hydrogen pressures compared to (partially) disordered samples [17]. Disordered $Fe_{0.25}Pd_{0.75}$ needs more than two orders of magnitude higher hydrogen pressure to obtain the same electrical resistivity as found in ordered $FePd_3$ [18]. The position of hydrogen atoms in $FePd_3H_x$ is not known yet.

In this work, we employ *in situ* studies to show the influence of moderate hydrogen pressures on the order–disorder transition in $FePd_3$, thus complementing studies of hydrogen absorption of $FePd_3$ at high hydrogen pressures [17]. *In situ* neutron powder diffraction, as an established method [19,20], was used to determine the level of atomic disorder, the magnetic moment and the amount of incorporated hydrogen.
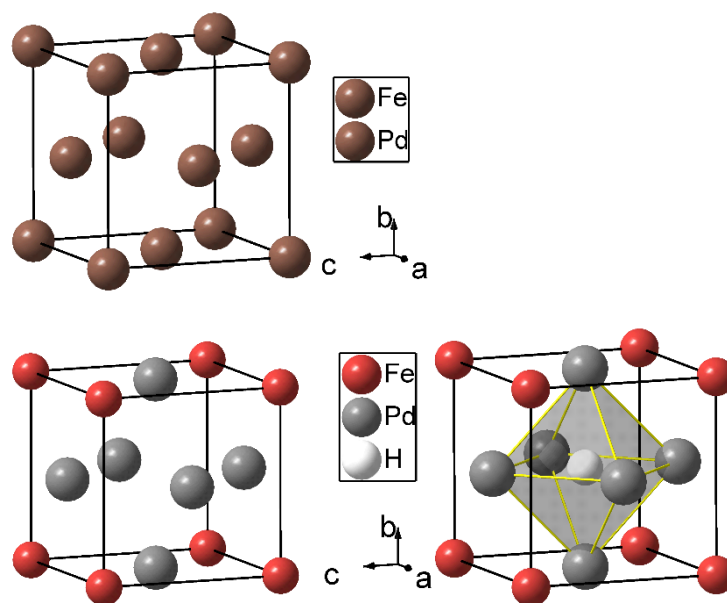
Figure 1. The crystal structures of $FePd_3$ in Cu type (left, disordered, $Fe_{0.25}Pd_{0.75}$, $Fm\bar{3}m$ [15]) and in $AuCu_3$ type (middle, ordered, $FePd_3$, $Pm\bar{3}m$ [15]) and the crystal structure of $FePd_3H_{0.05}$ in the cubic anti-perovskite type ($Pm\bar{3}m$ (this work)) with hydrogen atoms surrounded by six palladium atoms in an octahedral arrangement.

2. Materials and Methods

Synthesis and Chemical Analysis: Due to air sensitivity, iron was handled in an argon-filled glove box. Disordered $Fe_{0.25}Pd_{0.75}$ was synthesized from stoichiometric amounts of palladium powder (99.95%, $\leq$150 µm, Goodfellow) and iron granules (99.98%, 1–2 mm, abcr) in sealed silica glass ampoules under argon atmosphere. The mixture was heated to 1423 K (100 K h^{-1} heating rate) for 48 h and afterward quenched in air. The ordered compound was synthesized analogously; however, one small crystal of iodine (resublimed, Merck) was added as a mineralizing agent. This mixture was heated to 923 K (100 K h^{-1} heating rate) for 7 d in a sealed silica ampoule. A further sample was afterward annealed for one month at 773 K. The products were ground in a mortar after cooling.

Iodine was removed by sublimation to the opposite side of the ampoule. Chemical analyses were performed by an EDX INCA SYSTEM from Oxford Instruments, mounted on a Zeiss LEO 1530 scanning electron microscope, with an acceleration voltage of 20 kV and a working distance of 15 mm.

Thermal Analysis: Differential scanning calorimetry (DSC) was performed under hydrogen pressure on a DSC HP 2+ (Mettler Toledo) equipped with a gas pressure chamber. An amount of 20 mg of the powdered sample was put in an aluminum crucible, which was closed with an aluminum lid. This was placed inside the pressure chamber, which was then purged several times with hydrogen gas, before filling to the final hydrogen gas pressure of 5.0 MPa. The sample was heated to 723 K with 10 K min^{-1}, held at this temperature for a minimum of 1 h and cooled to 300 K. Two runs were performed; afterward, the hydrogen pressure was released, the sample removed and structural characterization undertaken by XRPD.

Ex situ **X-ray Powder Diffraction (XRPD):** X-ray powder diffraction data from flat transmission samples were collected on a G670 diffractometer (Huber, Rimsting, Germany) with Mo-K$_{\alpha 1}$ radiation (70.926 pm) and from flat reflection samples on a SmartLab powder high-resolution X-ray powder diffractometer (Rigaku, Tokyo, Japan) with a HyPix-3000 two-dimensional semiconductor detector using Co-K$_\alpha$ radiation with parallel beam. The instrumental resolution function and the wavelength distribution were determined using a measurement on an external silicon NIST640d standard sample. The wavelengths were found to be 178.9789(4) pm and 179.3625(4) pm, close to the usual values for Co-K$_{\alpha 1}$ and Co-K$_{\alpha 2}$; the difference was caused by optical components of the diffractometer affecting the wavelength distribution.

In situ **X-ray Powder Diffraction:** *In situ* X-ray powder diffraction was performed on a SmartLab powder high-resolution X-ray powder diffractometer (Rigaku, Tokyo, Japan) in an Anton Paar XRK 900 reaction chamber (Graz, Austria) with 0.5 MPa hydrogen pressure (H$_2$, Air Liquide, 99.9%) and Co-K$_\alpha$ radiation with parallel beam on a flat FePd$_3$ specimen on top of an Al$_2$O$_3$ layer.

Ex situ **Neutron Powder Diffraction (NPD):** Neutron powder diffraction was carried out at the Institute Laue-Langevin in Grenoble, France, with a high-flux diffractometer D20 in high-resolution mode. Powdered samples ($\approx$1 cm^{-3}) were held in air-tight vanadium containers with 6 mm inner diameter and were each measured for 15 min. The wavelength $\lambda = 186.80(2)$ pm was calibrated using an external silicon NIST640b standard sample in a 5 mm vanadium container. Deuterides rather than hydrides were used to avoid the high incoherent scattering of ^{1}H.

In situ **Neutron Powder Diffraction:** *In situ* neutron powder diffraction (NPD) was performed on a high-intensity two-axis diffractometer D20 at the Institute Laue-Langevin (ILL), Grenoble, France. Time-resolved neutron diffraction data were collected under deuterium pressure and heating by two lasers. These *in situ* experiments were carried out in (leuco-)sapphire single-crystal cells with 6 mm inner diameter connected to a gas supply system. The details are given elsewhere [19,20]. The sample cell was filled with FePd$_3$ and attached to the gas supply system, which was subsequently evacuated. The reactions were performed under various deuterium pressures (D$_2$, Air Liquide, 99.8% isotope purity). Data sets were obtained with 2 min time resolution. They are presented with an additional

internal raw label (NUMOR), referring to proposal 5-24-613 [21]. For the *in situ* studies, NUMORs 131613–131859 were used.

Rietveld Refinement: Rietveld refinements [22,23] were performed using FullProf [24] and Topas [25]. Deuterium atoms were located by difference Fourier analysis. Simultaneous refinements of $FePd_3$ based on XRPD data and neutron powder diffraction data were performed with constrained mixed occupation parameters to reduce correlation with the ordered magnetic moment of the iron atoms. Further details of the crystal structure investigations may be obtained from FIZ Karlsruhe, 76344 Eggenstein-Leopoldshafen, Germany (fax: (+49)7247-808-666; e-mail: crysdata@fiz-karlsruhe.de), on quoting the deposition number CSD-2163436.

3. Results

For reasons of clarity and simplification, partially disordered $FePd_3$ (typically with between 10% and 20% palladium atoms on iron sites and vice versa, *vide infra*) is referred to as ordered, and the completely disordered $Fe_{0.25}Pd_{0.75}$, with statistical distribution of iron and palladium atoms as disordered in the following text. The term hydride is used to include all hydrogen isotopes, unless indicated otherwise, e.g., for deuterides used in neutron diffraction experiments. Because of the small amount of dissolved hydrogen (deuterium), these phases may also be seen as solid solutions of hydrogen (deuterium) in $FePd_3$.

3.1. Synthesis and Chemical Analysis

The intermetallic compound $FePd_3$ was synthesized from the elements. To facilitate the ordering of the metal atoms, iodine was added as a mineralizing agent. The annealed and quenched samples were gray powders with a metallic luster. Based on chemical analysis, the empirical formulae $Fe_{0.97(13)}Pd_{3.03(13)}$ for the ordered and $Fe_{1.0(2)}Pd_{3.0(2)}$ for the disordered phase were determined, with values averaged from at least 20 energy dispersive X-ray (EDX) spectra of each. Based on these results, we assign the same sum formula $FePd_3$ for both the ordered and the disordered phase. We distinguish them by nomenclature, i.e., $FePd_3$ for the (partially) ordered and $Fe_{0.25}Pd_{0.75}$ for the disordered phase. The products are stable in air. The powder particles align with the magnetic field of a permanent magnet.

3.2. X-ray Diffraction and Thermal Analysis

X-ray diffraction is well suited to tracking down unit cell volume changes due to hydrogen uptake and to distinguishing between iron and palladium atoms, i.e., to investigating the atomic order. X-ray powder diffraction patterns of ordered $FePd_3$ exhibit anisotropic reflection broadening (Figure A1). Reflections common to both disordered (Cu type, $Fm\bar{3}m$) and ordered (AuCu$_3$ type, $Pm\bar{3}m$) are sharp (*hkl* all even or all odd), whereas those extinct by *F* centering and seen only in the ordered phase are considerably broader (*hkl* mixed even and odd), e.g., 100 with a half width at full maximum of 0.785°, 111 with 0.188°. This broadening can be attributed to small ordered domains joined by anti-phase boundaries to larger crystallites. This effect is also present in cubic $MnPd_3$ [26]. In the Rietveld refinement, the anisotropic reflection broadening was modeled by dividing the diffraction data set into two patterns with different regions of the 2θ range—one containing only reflections with *hkl* all even or all odd, and one containing all the others, i.e., those with *hkl* mixed even and odd (Figure A1 and Table A1). Each of the two patterns was treated independently in terms of profile parameters but constrained in terms of crystal structure parameters and scale factors. The refinement of occupation parameters (site occupation factors, *SOF*) for the 1*a* and 3*c* sites, with a stoichiometric constraint on the sum formula $FePd_3$, yielded *SOF*(Fe) = 0.876(2) at Wyckoff position 1*a*, i.e., about 12% palladium at iron sites (Figures 2 and A1, and Tables 1 and A1). The long-time annealed sample yielded *SOF*(Fe) = 0.99(2) instead, i.e., it was fully ordered (Figure A2 and Table A2).
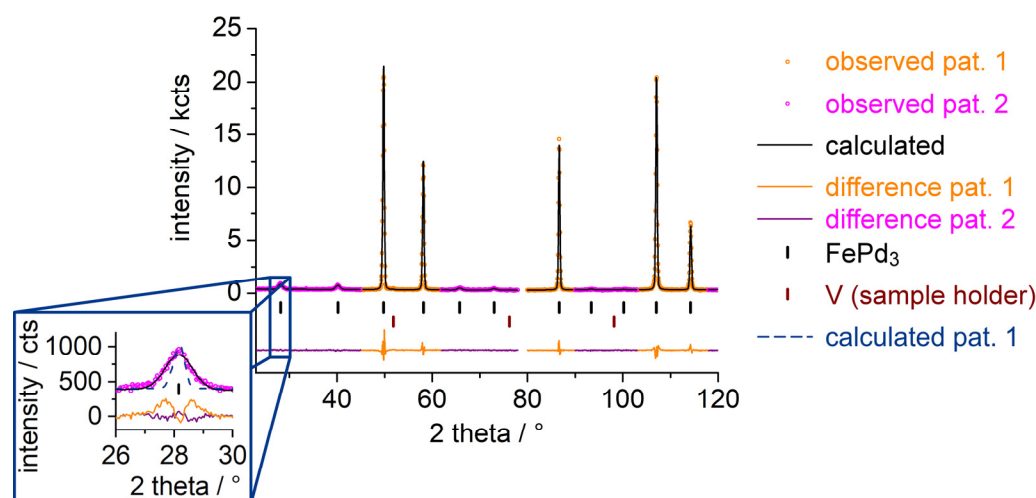
Figure 2. Simultaneous Rietveld refinement (X^2 = 1.97) of the crystal and magnetic structure of $FePd_3$ ($AuCu_3$ type, $Pm\bar{3}m$, a = 385.204(6) pm, R_{Bragg}(pat.1) = 2.13, R_{Bragg}(pat.2) = 6.73, R_{magn}(pat.1) = 2.26, R_{magn}(pat.2) = 6.12; for further details, see Tables 1 and A5 and the text) at 296(1) K based on neutron powder diffraction data (NUMOR 131401 [21], λ =186.80(2) pm, D20 ILL, Grenoble, R_p(pat.1) = 0.057, R_p(pat.2) = 0.069, R_{wp}(pat.1) = 0.080, R_{wp}(pat.2) = 0.087, background corrected: R'_p(pat.1) = 0.083, R'_p(pat.2) = 0.667, R'_{wp}(pat.1) = 0.100, R'_{wp}(pat.2) = 0.410) and XRPD data (Figure A1, Co-Kα radiation, Smart Lab, R_p(pat.3) = 0.105, R_p(pat.4) = 0.102, R_{wp}(pat.3) = 0.150, R_{wp}(pat.4) = 0.140, R'_p(pat.3) = 0.160, R'_p(pat.4) = 1.90, R'_{wp}(pat.3) = 0.192, R'_{wp}(pat.4) = 0.804) using FullProf [24]. The inset shows the broadening of pattern 2 reflections through a comparison of intensities for 100 reflections calculated with the reflection width of pattern 1 (blue dashed line) and the reflection width of pattern 2 (black line) with the respective difference plot.

Table 1. Crystal structure parameters of $FePd_3$ ($Pm\bar{3}m$) based on neutron powder diffraction (a = 385.204(6) pm, μ_{Fe} = 2.3(2) μ_B; see Figure 2) and XRPD (a = 385.390(3) pm; compare Figure A1) at 296(1) K.

Atom	Wyckoff Position	x	y	z	$B_{iso1}/10^{-4}$ pm^2 NPD	$B_{iso2}/10^{-4}$ pm^2 XRPD	SOF
Fe1	$1a$	0	0	0	2.17(8)	0.19(4)	0.876(2)
Fe2	$3c$	0	$\frac{1}{2}$	$\frac{1}{2}$	1.11(12)	0.88(4)	$(1 - SOF(Fe1))/3$
Pd1	$1a$	0	0	0	$B_{iso1}(Fe1)$	$B_{iso2}(Fe1)$	$1 - SOF(Fe1)$
Pd2	$3c$	0	$\frac{1}{2}$	$\frac{1}{2}$	$B_{iso1}(Fe2)$	$B_{iso2}(Fe2)$	$1 - (1 - SOF(Fe1))/3$

The thermal analysis (DSC, $p_{start}(H_2)$ = 5.00(2) MPa, T_{max} = 723 K) of the $FePd_3$ phase shows no thermal signal (Figure A3). However, the unit cell increases by 0.08% ($a(FePd_3)$ = 385.330(5) pm, $a(FePd_3H_x)$ = 385.433(3) pm, according to Rietveld analysis of XRPD data), and the disorder increases as well (SOF(Fe, $1a$, $FePd_3$) = 0.909(10), SOF(Fe, $1a$, $FePd_3H_x$) = 0.841(12)) based on X-ray powder diffraction (Mo-K$_{\alpha1}$ radiation) before and after DSC (Figure A4).

In situ X-ray diffraction at 0.50(5) MPa hydrogen pressure on the long-time annealed $FePd_3$ sample shows a decrease in the level of atomic order. After the *in situ* chamber was flushed with hydrogen to a pressure of 0.50(5) MPa, SOF(Fe) decreased from 0.99(2) to 0.877(2). Furthermore, the cell volume increased by 0.2% ($a(FePd_3)$ = 385.412(4) pm; $a(FePd_3H_x)$ = 385.631(4) pm), indicating hydrogen uptake at room temperature. In the subsequent heating and cooling steps of 50 K to a maximum temperature of 550 K, SOF stays constant, and the lattice parameters change reversibly with temperature (Figures A5 and A6, and Tables A3 and A4), indicating that the hydrogen-induced disorder occurs at room temperature and does not proceed further at elevated temperatures.

3.3. Neutron Diffraction
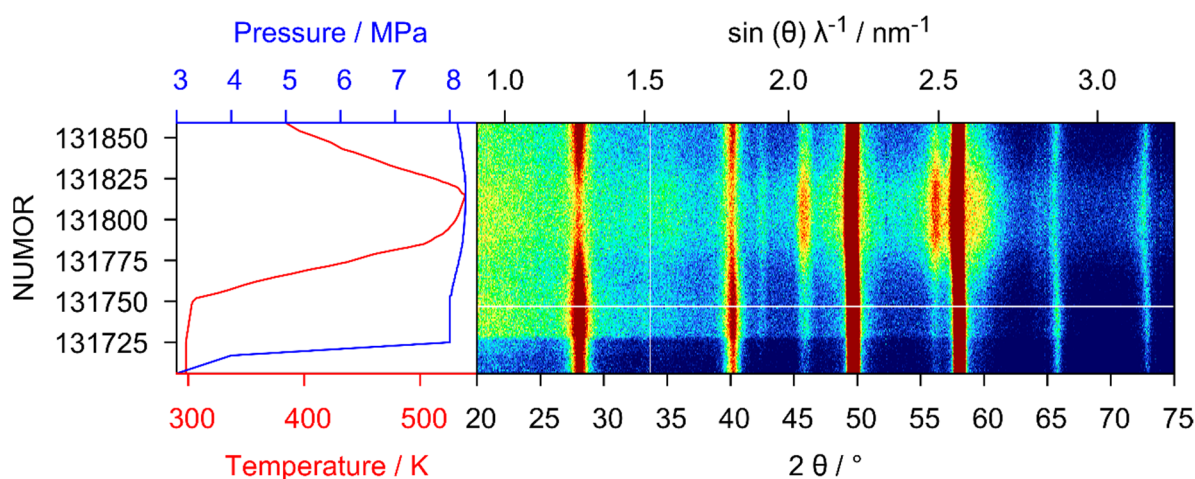
3.3.1. *Ex Situ* Neutron Diffraction

The disordered $Fe_{0.25}Pd_{0.75}$ sample shows no significant cell volume increase (Figure A7, a_{before} = 385.12(4) pm, a_{after} = 385.18(2) pm) when subjected to deuterium gas ($p_{max}(D_2)$ = 8.3 MPa, T_{max} = 558 K). Furthermore, no deuterium atoms can be found in the crystal structure (zero occupation at Wyckoff position $4b$, $\frac{1}{2}$, $\frac{1}{2}$, $\frac{1}{2}$; analogous to PdH [27]), and the iron and palladium atoms remain disordered. Therefore, we conclude that disordered $Fe_{0.25}Pd_{0.75}$ does not take up hydrogen under the given conditions. This result is in accordance with hydrogenation studies under higher pressures [17].

The neutron diffraction pattern of ordered $FePd_3$ shows the same anisotropic reflection broadening (Figure 2) as observed with XRPD (*vide supra* and Figure A1). For modeling in Rietveld refinements, the same strategy of dividing into two patterns as described above for XRPD was used. Each of the patterns was constrained to the respective XRPD pattern in a simultaneous refinement on X-ray and neutron diffraction data. Please note that here, and for the following refinements, the residual values for pattern 2 are quite high because of low intensities and broad reflections (purple line in Figures 2, A1, A2, A4 and A7–A27). Approximately 12% palladium atoms on iron sites were found with a fixed composition of $FePd_3$ as a constraint (Table 1). The refined value for the magnetic moment of the iron atoms of 2.3(2) μ_B along [001] is in accordance with the literature data (μ_{Fe} = 2.73(13) μ_B [28]) within two standard uncertainties. Palladium atoms were not included in the magnetic structure, since the refinements did not converge, indicating small μ_{Pd} values. This is in line with the small magnetic moments of palladium atoms in $FePd_3$ found earlier (μ_{Pd} = 0.35 μ_B [29]).

The unit cell volume of ordered $FePd_3$ expanded by 0.20% upon deuterium uptake ($a(FePd_3)$ = 385.204(3) pm, $a(FePd_3D_{0.047(9)})$ = 385.372(2) pm). Deuterium atoms were localized by difference Fourier analysis. For the refinement of deuterium occupation, the magnetic moment of iron was fixed at 2.344 μ_B due to convergence problems. Two possible deuterium sites were tested by Rietveld refinement. The Wyckoff position $3d$ $(0\ 0\ \frac{1}{2})$ yields a negative deuterium occupation and is thus considered to be empty. The occupation of deuterium in $[Pd_6]$ octahedral voids at Wyckoff position $1b$ $(\frac{1}{2}\ \frac{1}{2}\ \frac{1}{2})$ was refined to 0.047(9). We therefore conclude the deuteride to be $FePd_3D_{0.047(9)}$ with an anti-perovskite type structure (Figure 1).

3.3.2. *In Situ* Neutron Diffraction

To study the influence of structural order in $FePd_3$ on hydrogenation properties, *in situ* neutron powder diffraction on an ordered sample using deuterium in a sapphire single-crystal cell was performed (Figure 3). Deuterium gas pressure was slowly increased up to 8.0 MPa before raising the temperature to about 550 K. After maintaining the temperature for one hour, the cell was cooled to room temperature under deuterium pressure. As seen in the 2D plot, the intensities of reflections with *hkl* mixed even and odd (e.g., at 2θ = 28°, 40°, 66°, 73°) decrease with increasing temperature. This observation indicates an increasing level of disorder and decreasing ordered magnetic moment. Reflections (2θ = 42.4°; 45.6°; 56.1°) at high temperatures are single-crystal reflections from the sapphire cell that shift into the range of the detector due to thermal expansion.

Figure 3. *In situ* neutron powder diffraction data (NUMOR 13,1706−13,1859 [21]) of the deuteration of ordered $FePd_3$ taken with diffractometer D20 (Grenoble, France) at λ = 186.80(2) Å in a single-crystal sapphire cell [19,20] under various temperature and deuterium pressure conditions. Intensities are in false colors.

The Rietveld refinements of selected NUMORs during the isothermal deuterium pressure increase were performed with fixed magnetic moments. Magnetic investigations of isotypic $FePd_3B_x$ show that only the ordered magnetic moment of the immediate boron environment (only Pd atoms) is changed upon boron incorporation [30], while the magnetic moment of the Fe atoms is not affected. Therefore, we consider fixing the magnetic moments of iron atoms to be an appropriate approximation. The refinements during the quasi-isobaric temperature variation were performed with fixed mixed occupancy. This is because *in situ* XRPD at 0.5 MPa hydrogen pressure showed no significant change, and a simultaneous refinement of the magnetic moment, the hydrogen occupation, and the mixed occupancy of the metal atoms did not converge. The lattice parameter *a* of $FePd_3D_x$ increases with rising deuterium pressure (Figure 4, left), which is reflected in the increasing deuterium content. At 8 MPa deuterium pressure, the composition $FePd_3D_{0.047(9)}$ is reached. The disorder increases with deuterium uptake, as seen from the iron occupation at Wyckoff position 1*a* decreasing from 0.875(3) to 0.794(3). In the heating step (T_{max} = 539 K) at 8.2(2) MPa deuterium pressure, the lattice parameter *a* increases almost linearly, and the deuterium content does not change significantly (Figure 4). The ordered magnetic moment decreases with increasing temperature to zero. The data were fitted with a function for a second-order transition based on the Landau theory with the magnetic moment as the order parameter:

$$\mu_{ord.} = A \left(\frac{T_C - T}{T_C} \right)^{\beta}$$

The resulting Curie temperature, T_C, is 495(8) K, and the critical exponent β equals 0.28(5) (Figure 4). The ordered magnetic moments at temperatures above the Curie temperature are not significantly different from zero or are set to zero at the maximum temperature of 539 K. All observed trends are fully reversible during the cooling step.
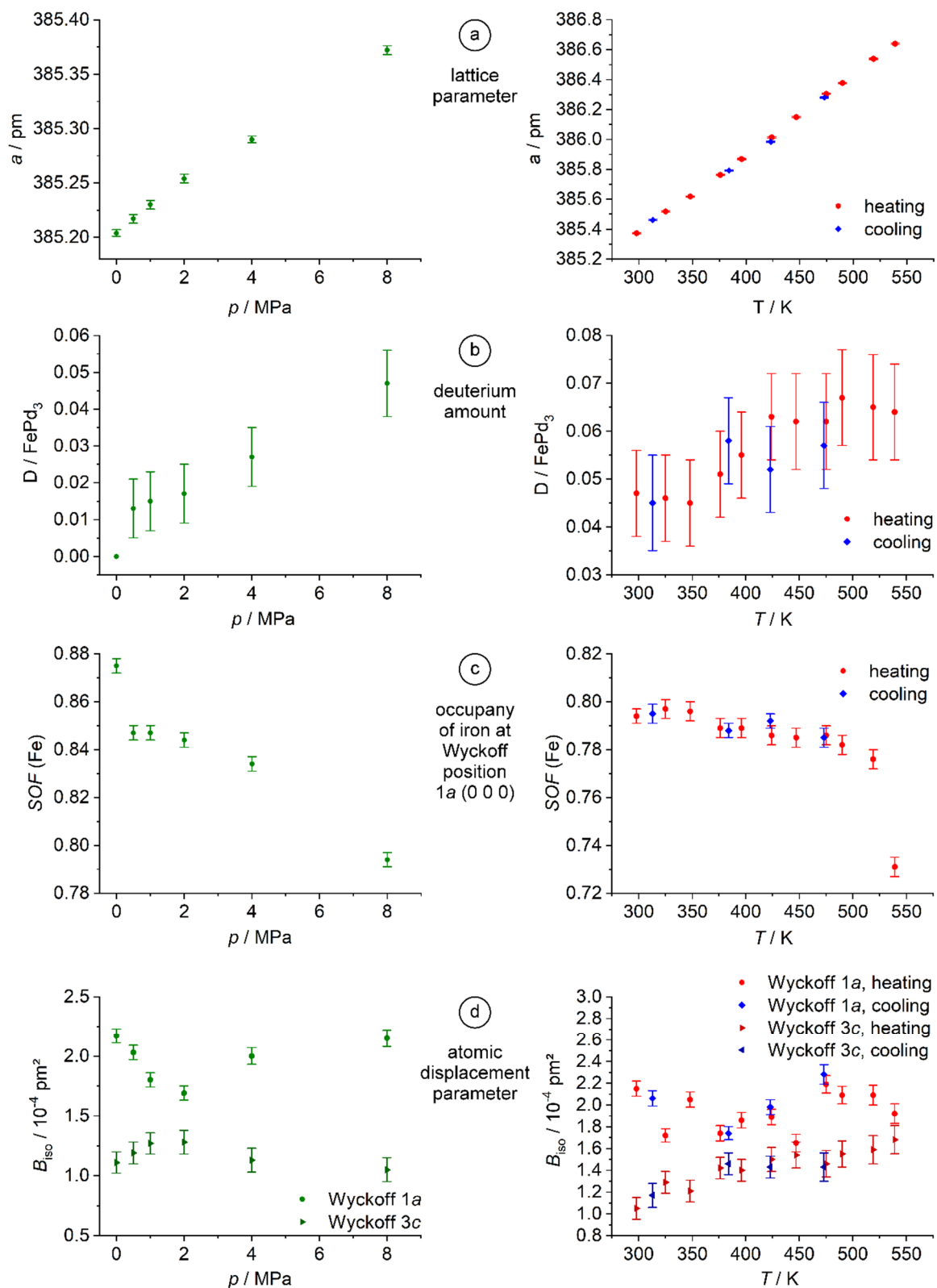
Figure 4. Refined structural parameters of ordered $FePd_3$ during isothermal increase in deuterium pressure (left, NUMOR 131613–131746 [21], T = 298(2) K) and isobaric variation of the temperature (right, NUMOR 131746–131894 [21], $p(D_2)$ = 8.2(2) MPa) based on *in situ* neutron powder diffraction data: lattice parameter (**a**), deuterium content per formula unit (**b**), *SOF* of iron at Wyckoff position 1*a* (**c**) and atomic displacement parameters of the metal atoms (**d**). Error bars represent $\pm\sigma$.

4. Discussion

The atomic order in $FePd_3$ can be controlled via the synthesis protocol, most easily by using iodine as a mineralizing agent. Its use allows full atomic order in one month as compared to 91% order in two months [16]. This method is well known for its potential to promote single-crystal growth [31,32], the synthesis of metastable compounds [32] or single-phase ordered compounds with shorter annealing times [31].

The magnetic moment of 2.3(2) μ_B of $FePd_3$ determined by refinement of neutron diffraction data differs somewhat from the literature values (μ_{Fe} = 2.73(13) μ_B [28]); however, the difference is less than two combined standard uncertainties. The difference may also be caused by varying disorder in $FePd_3$, which was not taken into account in early studies [28,33]. The Curie temperature of 495(8) K, determined by a second-order transition fit (Figure 5), is in accordance with the literature (T_c = 499 K [6]). The determined critical exponent of this fit (β = 0.28(5)) is close (less than two standard uncertainties apart) to the expected values of a 3D Ising model (β = 0.325) and a 3D Heisenberg model (β = 0.365) but far from the mean-field model (β = 0.5) [34]. This is in perfect agreement with a short-range interaction as typical for a magnetic exchange. The disparity between this and previous investigations reporting on a Heisenberg magnet with a critical exponent of 0.371 [6] may be explained by the method of determination. The ordered magnetic moment in this study is only refined in the 001 direction, resulting in a bias toward the 3D Ising model. Furthermore, the uncertainties are relatively high due to the correlation of the hydrogen occupation, the mixed occupation and the ordered magnetic moment.
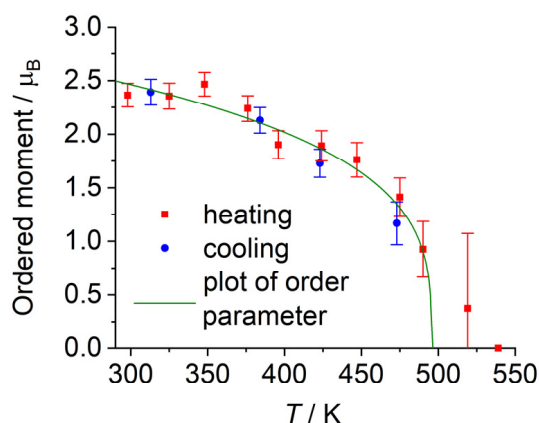
Figure 5. Temperature dependence of refined magnetic moment with fixed occupation (SOF(Fe,1a) = 0.798) in ordered $FePd_3$ under isobaric conditions ($p(D_2)$ = 8.2(2) MPa) based on *in situ* neutron powder diffraction data (see Figure 3). Green line shows the fitted function of the model of second-order phase transition ($\mu_{ord.}$ = 3.2(2)$\mu_B \left(\frac{495(8)\ K - T}{495(8)\ K} \right)^{0.28(5)}$).

Deuterium occupies exclusively [Pd_6] octahedral voids in a statistical manner with small occupation parameters. The small deuterium contents are in accordance with studies at high gas pressures [17] (Figure 6, left). The Pd-D distances are between 192.644(2) pm and 192.686(2) pm for $FePd_3D_{0.013(8)}$ and $FePd_3D_{0.047(9)}$, respectively, and comparable to known hydrides of MPd_3 compounds, such as $MnPd_3H_{0.61}$ (190.0 pm $\leq d$(Pd-H) $\leq$ 197.6 pm) [35].
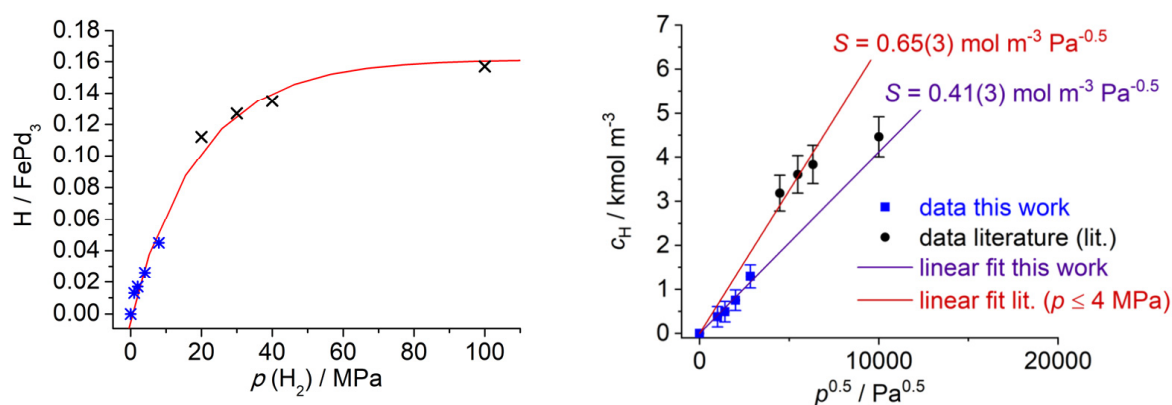
Figure 6. Plot of hydrogen pressure vs. hydrogen content (left) and Sieverts' law (right, $c_H = S\sqrt{p}$ [36]) of FePd$_3$H$_x$. Black symbols mark data from the literature [17], blue symbols from this work. Red line on the left-hand side shows an empirical fitted function ($x = -0.161(5)\mathrm{e}^{-0.050(5)p} + 0.161(4)$) and red and purple lines a linear fit based on Sieverts' law.

FePd$_3$ takes up much less hydrogen than, i.e., MgPd$_3$ [20], MnPd$_3$ [35,37] or InPd$_3$ [38]. This is in accordance with a proposed structure map correlating electronegativity and atomic radius of the metal M with the hydrogen content of MPd$_3$H$_x$ [39]. Iron, with quite a small atomic radius and an electronegativity of 1.6, is predicted to take up small amounts of hydrogen, which is confirmed in this study. Furthermore, the density of states at the Fermi level of FePd$_3$ (6.2 [40] or 11.1 states eV^{-1} atom^{-1} [41]) is remarkably high compared to other MPd$_3$ compounds crystallizing in the AuCu$_3$ type, such as MgPd$_3$ (1.13 states eV^{-1} atom^{-1} [42]), MnPd$_3$ (2.18 [43] or 2.84 states eV^{-1} atom^{-1} [44]) and InPd$_3$ (3.3 states eV^{-1} atom^{-1} [45]), which might also have an impact on the hydrogen uptake capacity. At room temperature, the hydrogenation follows Sieverts' law [36] (Figure 6, right), with low pressure (this work) and high pressure data [17] differing somewhat (Figure 6). The moderate fit and higher error in fit parameters for the high pressure data may be caused by increasing hydrogen–hydrogen interaction in the solid solution and larger differences between fugacity and pressure, the latter of which was used here as an approximation.

To compare the possible hydrogenation of ordered and disordered FePd$_3$, it is useful to look at the maximum hydrogen content of both structure types. The unit cell of MPd$_3$ compounds in the AuCu$_3$ type contains one [Pd$_6$] and three [M_2Pd$_4$] octahedral voids. Therefore, the probability of a [Pd$_6$] octahedral void is 0.25, yielding the formula MPd$_3$H for a maximum occupation of hydrogen in [Pd$_6$] sites. For disordered MPd$_3$ compounds crystallizing in the Cu type, the probability of a [Pd$_6$] octahedral void is 0.178 (=0.75^6), assuming a 75% probability of finding a palladium atom at any position in the crystal structure. A maximum hydrogen occupation using only [Pd$_6$] sites yields the formula MPd$_3$H$_{0.712}$. According to this consideration, the ordered compound may absorb more hydrogen if only [Pd$_6$] sites are involved. It is well known that hydrogen uptake in disordered FePd$_3$ is indeed less than that for ordered FePd$_3$ [17]. In this regard, it is remarkable that the disorder in FePd$_3$H$_x$ increases with hydrogen uptake despite the statistical decrease in [Pd$_6$] octahedral sites. Furthermore, the disorder reversibly increases with temperature, with near constant hydrogen content. The preference of [Pd$_6$] sites for hydrogen atoms can be inferred from many examples of hydrogenation reactions of MPd$_3$ compounds structurally related to cubic close packing. The thermodynamic driving force for hydrogen-induced rearrangements (from TiAl$_3$ type or ZrAl$_3$ type to AuCu$_3$ type) arises from the preference for Pd-H bonding and, consequently, an increase in the number of [Pd$_6$] octahedral voids [46]. Furthermore, other interstitial FePd$_3$ compounds, such as FePd$_3$B$_x$, also prefer [Pd$_6$] octahedral sites for the interstitial atoms [30]. The immediate environment of absorbed hydrogen is responsible for the hydrogen solubility in metals

and intermetallic compounds [47]. Under the assumption of a preference of hydrogen atoms for $[Pd_6]$ octahedra, the unexpected increasing disorder upon hydrogenation may be understood in terms of local short-range order of formed HPd_6 octahedra and a lack of long-range crystallographic order.

The findings on the magnetic and structural details of $FePd_3$ and its hydrides show the complex interplay between hydrogen uptake, atomic and magnetic order in intermetallics. This raises questions on the validity of the assumption of constant atomic order, which is often made for investigations on the effects of hydrogen incorporation on magnetic properties, and calls for further investigations on this fascinating subject.

5. Conclusions

The use of iodine as a mineralizing agent decreases the annealing time and enables higher ordering of metal atoms in the synthesis of $FePd_3$. At moderate hydrogen pressures ($p \leq 8$ MPa), disordered $Fe_{0.25}Pd_{0.75}$ absorbs a negligible amount of hydrogen, and ordered $FePd_3$ forms the hydride $FePd_3H_{0.047(9)}$. Hydrogen is incorporated at $[Pd_6]$ octahedral voids, and the hydrogenation follows Sieverts' law. During heating, the ordered magnetic moment decreases, and $FePd_3H_x$ behaves like a 3D Ising or Heisenberg magnet. Simultaneously, the disorder of the metal atoms increases slightly. All temperature-dependent effects are fully reversible. Hydride formation in $FePd_3$ influences crystallographic and magnetic order alike. The citation of Carl G. Jung "In all chaos there is a cosmos, in all disorder a secret order" [48] can be understood as order only arising from chaos. In contrast to that, hydrogen seems to enhance the metal diffusion in $FePd_3$, resulting in long-range disorder arising from local order of the immediate hydrogen environment. This induced metal diffusion and the resulting change in the arrangement of the metal atoms at the surface might raise interest in catalysis.
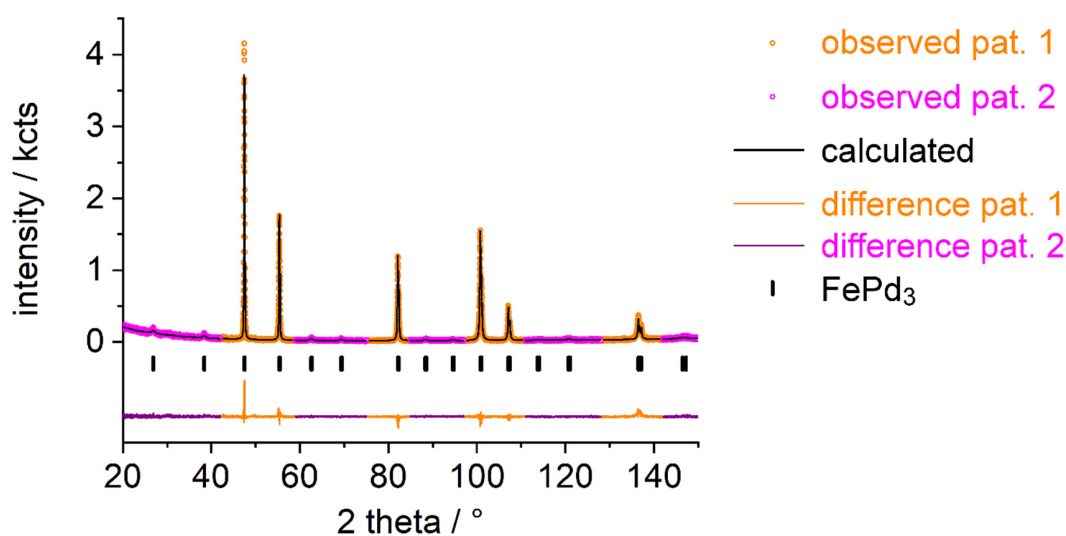
Author Contributions: Conceptualization, A.G. and H.K.; methodology, A.G., S.C.S., T.C.H. and H.K.; software, A.G. and T.C.H.; validation, A.G., S.C.S., T.C.H. and H.K.; formal analysis, A.G.; investigation, A.G., S.C.S., T.C.H. and H.K.; resources, H.K. and T.C.H.; data curation, A.G. and T.C.H.; writing—original draft preparation, A.G.; writing—review and editing, A.G., S.C.S., T.C.H. and H.K.; visualization, A.G.; supervision, H.K.; project administration, A.G. and H.K.; funding acquisition, H.K. All authors have read and agreed to the published version of the manuscript.
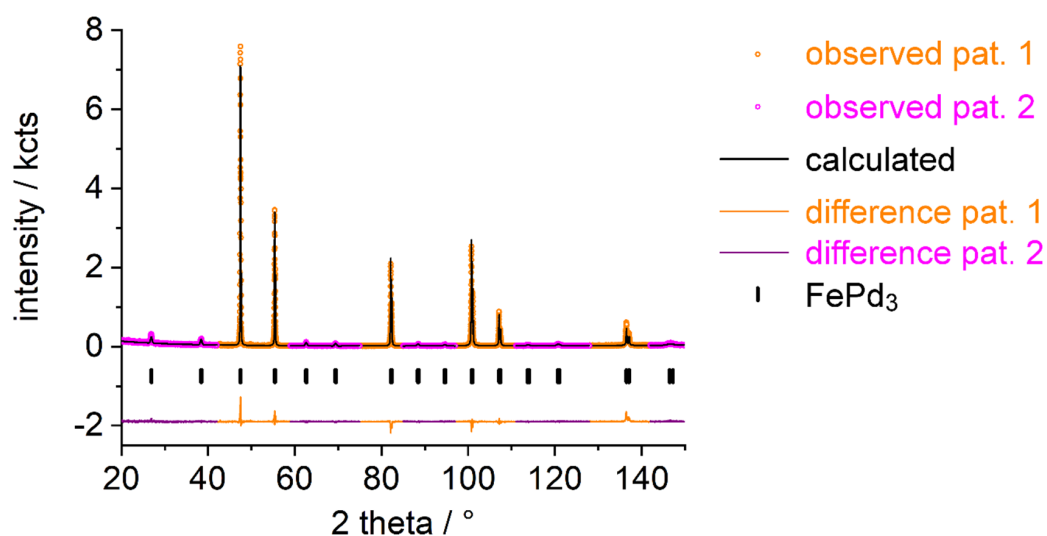
Appendix A

Figure A1. Rietveld refinement of the crystal structure of ordered $FePd_3$ (AuCu$_3$ type, $Pm\overline{3}m$, $a = 385.380(5)$ pm, R_{Bragg}(pat.1) = 5.45, R_{Bragg}(pat.2) = 49.4; for further details, see Table A1) at 296(1) K based on XRPD powder diffraction data (Co-Kα radiation, Smart Lab, R_{p}(pat.1) = 0.105, R_{p}(pat.2) = 0.102, R_{wp}(pat.1) = 0.150, R_{wp}(pat.2) = 0.140, X^2 = 2.24, background corrected: R'_{p}(pat.1) = 0.124, R'_{p}(pat.2) = 1.90, R'_{wp}(pat.1) = 0.163, R'_{wp}(pat.2) = 0.804) using FullProf [24].

Table A1. Crystal structure parameters of $FePd_3$ ($Pm\overline{3}m$, $a = 385.380(5)$ pm) based on XRPD data (see Figure A1) at 296(1) K.

| Atom	Wyckoff Position	x	y	z	$B_{\text{iso}}/10^{-4}$ pm^2	SOF
Fe1	1a	0	0	0	0.18(4)	0.87(2)
Fe2	3c	0	$\frac{1}{2}$	$\frac{1}{2}$	0.88(1)	$(1 - SOF(\text{Fe1}))/3$
Pd1	1a	0	0	0	$B_{\text{iso}}(\text{Fe1})$	$1 - SOF(\text{Fe1})$
Pd2	3c	0	$\frac{1}{2}$	$\frac{1}{2}$	$B_{\text{iso}}(\text{Fe2})$	$1 - (1 - SOF(\text{Fe1}))/3$

Figure A2. Rietveld refinement of the crystal structure of ordered $FePd_3$ (long-time annealed sample, AuCu$_3$ type, $Pm\overline{3}m$, $a = 385.412(4)$ pm, R_{Bragg}(pat.1) =8.01, R_{Bragg}(pat.2) = 27.1; for further details, see Table A2) at 296(1) K based on XRPD powder diffraction data (Co-Kα radiation, Smart Lab, R_{p}(pat.1) = 0.109, R_{p}(pat.2) = 0.125, R_{wp}(pat.1) = 0.161, R_{wp}(pat.2) = 0.173, X^2 = 3.79, background corrected: R'_{p}(pat.1) = 0.147, R'_{p}(pat.2) = 1.23, R'_{wp}(pat.1) = 0.161, R'_{wp}(pat.2) = 0.553) using FullProf [24].

Table A2. Crystal structure parameters of FePd$_3$ (long-time annealed sample, $Pm\bar{3}m$, a = 385.412(4) pm) based on XRPD data (see Figure A2) at 296(1) K.

| Atom	Wyckoff Position	x	y	z	$B_{iso}/10^{-4}$ pm^2	SOF [1]
Fe1	1a	0	0	0	1.5(2)	0.99(2)
Fe2	3c	0	$\frac{1}{2}$	$\frac{1}{2}$	1.88(4)	$(1 - SOF(\text{Fe1}))/3$
Pd1	1a	0	0	0	$B_{iso}(\text{Fe1})$	$1 - SOF(\text{Fe1})$
Pd2	3c	0	$\frac{1}{2}$	$\frac{1}{2}$	$B_{iso}(\text{Fe2})$	$1 - (1 - SOF(\text{Fe1}))/3$

[1] The stoichiometric ratio of Fe to Pd atoms was fixed at 1:3.
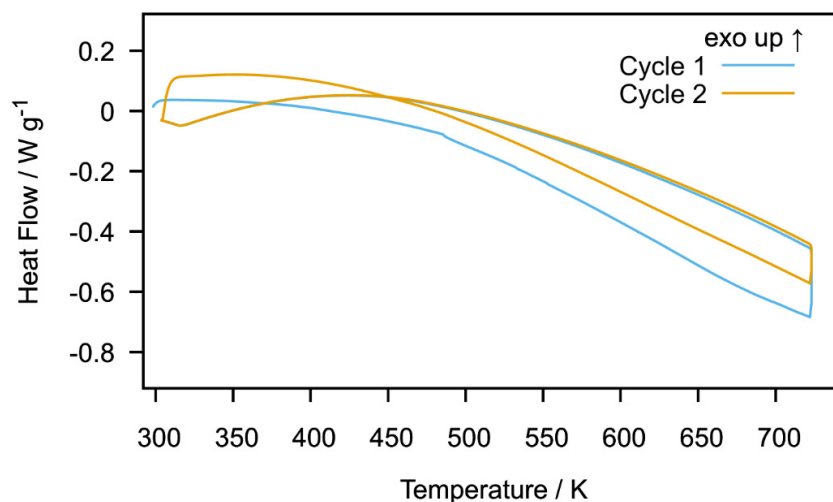

Figure A3. Differential scanning calorimetry (DSC) of ordered FePd$_3$ at 5.0 MPa hydrogen pressure.
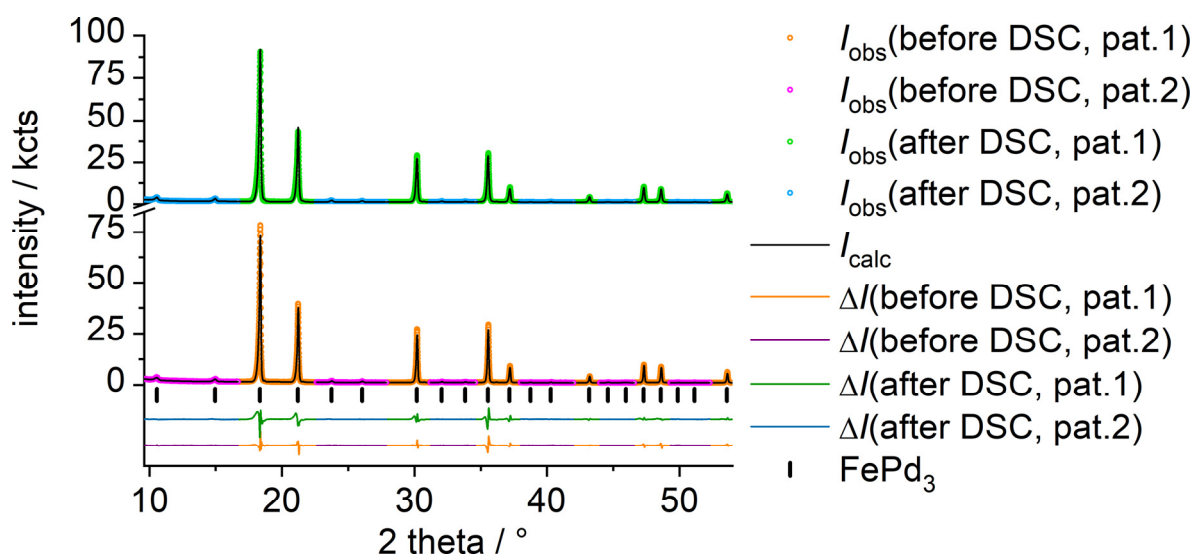
Figure A4. Rietveld refinement of the crystal structure of ordered FePd$_3$ before DSC (bottom, AuCu$_3$ type, $Pm\bar{3}m$, a = 385.330(5) pm, $SOF(\text{Fe}, 1a)$ = 0.909(10), $B_{iso}(1a)$ = 0.35(9) 10^{-4} pm^2, $B_{iso}(3c)$ = 0.91(2) 10^{-4} pm^2, R_{Bragg}(pat.1) = 2.83, R_{Bragg}(pat.2) = 2192, R_p(pat.1) = 0.089, R_p(pat.2) = 0.020, R_{wp}(pat.1) = 0.142, R_{wp}(pat.2) = 0.025, GOF = 5.09) and after DSC (top, AuCu$_3$ type, $Pm\bar{3}m$, a = 385.433(3) pm, $SOF(\text{Fe}, 1a)$ = 0.841(12), $B_{iso}(1a)$ = 0.96(12) 10^{-4} pm^2, $B_{iso}(3c)$ = 0.69(3) 10^{-4} pm^2, R_{Bragg}(pat.1) = 4.10, R_{Bragg}(pat.2) = 2150, R_p(pat.1) = 0.131, R_p(pat.2) = 0.024, R_{wp}(pat.1) = 0.189, R_{wp}(pat.2) = 0.030, GOF = 5.09) at 297(1) K based on XRPD powder diffraction data (Mo-K$_{\alpha 1}$ radiation, Huber G670) using Topas [25].
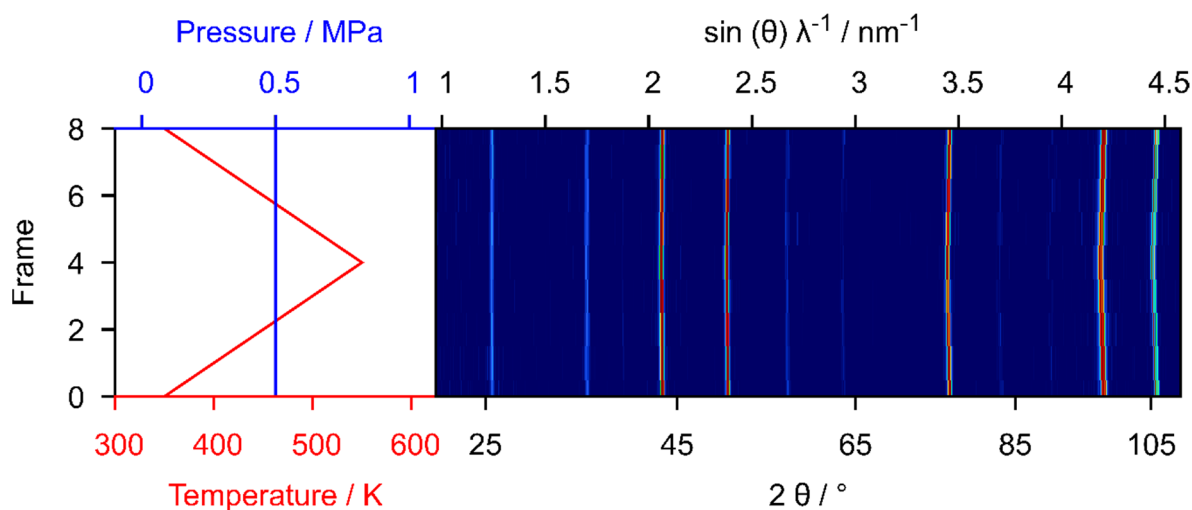
Figure A5. *In situ* X-ray powder diffraction data of the hydrogenation of ordered FePd$_3$ (long-time annealed sample) taken with SmartLab diffractometer in an XRK 900 reaction chamber with Co-Kα radiation under various temperatures and 0.5 MPa hydrogen pressure. λ_1 is used for sin (θ) λ^{-1} scale. Intensities are in false colors.
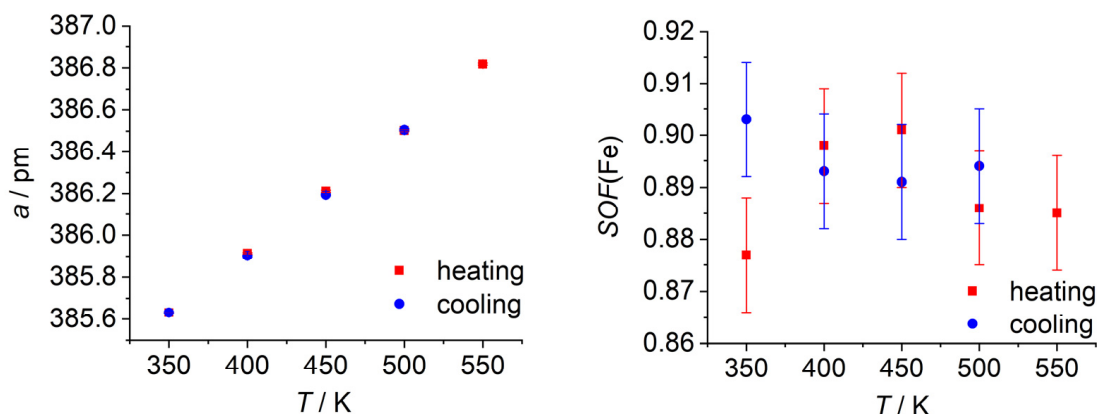
Figure A6. Refined structural parameters of ordered FePd$_3$ (long-time annealed sample, see Figure A5 and Tables A3 and A4) during isobaric variation of the temperature (p(H$_2$) = 0.50(5) MPa) based on *in situ* XRPD data: lattice parameter (left) and *SOF* of iron at Wyckoff position 1*a* (right). Error bars represent $\pm\sigma$.

Table A3. Conditions and refined parameters of the Rietveld refinement of FePd$_3$ (long-time annealed sample, $Pm\bar{3}m$) based on *in situ* XRPD data (see Figures A5 and A6, and Table A4) using Topas; X-ray absorption modeled with an overall B value of -4×10^{-4} pm^2 [25].

Frame	*T*/K	*p*/MPa	*a*/pm	*V*/10^6 pm^3	B_{iso}(1*a*)/10^{-4} pm^2	B_{iso}(3*c*)/10^{-4} pm^2	*SOF*(Fe, 1*a*) [1]
0	350 (2)	0.50 (5)	385.631 (4)	57.348 (2)	1.9 (2)	2.54 (4)	0.877 (11)
1	400 (2)	0.50 (5)	385.914 (4)	57.474 (2)	1.8 (2)	2.67 (4)	0.898 (11)
2	450 (2)	0.50 (5)	386.211 (5)	57.607 (2)	1.8 (2)	2.76 (5)	0.901 (11)
3	500 (2)	0.50 (5)	386.503 (5)	57.738 (2)	1.9 (2)	2.79 (5)	0.886 (11)
4	550 (2)	0.50 (5)	386.818 (5)	57.879 (2)	2.2 (2)	2.97 (5)	0.885 (11)
5	500 (2)	0.50 (5)	386.506 (5)	57.739 (2)	2.0 (2)	2.80 (5)	0.894 (11)
6	450 (2)	0.50 (5)	386.194 (4)	57.599 (2)	2.2 (2)	2.68 (4)	0.891 (11)
7	400 (2)	0.50 (5)	385.902 (4)	57.469 (2)	1.8 (2)	2.71 (4)	0.893 (11)
8	350 (2)	0.50 (5)	385.632 (4)	57.348 (2)	1.5 (2)	2.54 (4)	0.903 (11)

[1] The stoichiometric ratio of Fe to Pd atoms was fixed at 1:3.

Table A4. Residual parameters of the Rietveld refinement of FePd$_3$ (long-time annealed sample, $Pm\bar{3}m$) based on *in situ* XRPD data (see Figures A5 and A6, and Table A3) using Topas [25].

Frame	R_{p1}	R_{p2}	R_{wp1}	R_{wp2}	χ^2	R_{Bragg}
0	0.155	0.41	0.273	0.51	1.06	5.34
1	0.158	0.41	0.275	0.51	1.08	5.78
2	0.153	0.42	0.266	0.52	0.98	5.7
3	0.154	0.42	0.263	0.52	0.96	5.58
4	0.161	0.42	0.270	0.53	1.02	5.84
5	0.156	0.41	0.268	0.52	1.00	5.74
6	0.150	0.41	0.262	0.52	0.96	5.83
7	0.151	0.42	0.266	0.52	1.00	5.44
8	0.152	0.42	0.265	0.52	1.00	5.38
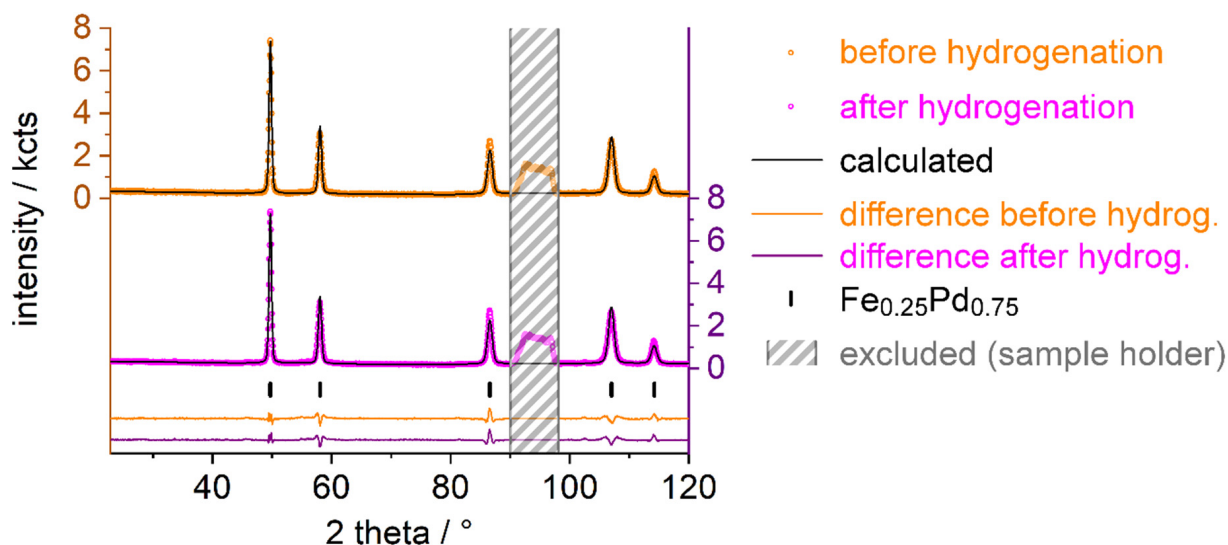
Figure A7. Rietveld refinement of the crystal structure of disordered Fe$_{0.25}$Pd$_{0.75}$ before hydrogenation (top, Cu type, $Fm\bar{3}m$, a = 385.12(4) pm, $B_{iso}(1a)$ = 1.52(5) 10^{-4} pm^2, R_{Bragg}(pat.1) = 3.39, R_p(pat.1) = 0.073, R_{wp}(pat.1) = 0.093, GOF = 2.54) and after hydrogenation ($p_{max}(D_2)$ = 8.3 MPa, T_{max} = 558 K) at 8.00(2) MPa deuterium pressure (bottom, Cu type, $Fm\bar{3}m$, a = 385.18(5) pm, $B_{iso}(1a)$ = 1.47(5) 10^{-4} pm^2, R_{Bragg}(pat.1) = 3.47, R_p(pat.1) = 0.065, R_{wp}(pat.1) = 0.084, GOF = 3.61) at 297(1) K based on neutron powder diffraction data (NUMORs 132451 and 132636 [21], λ = 186.80(2) pm, D20 ILL, Grenoble) using FullProf [24].

Table A5. Set constraints of the simultaneous Rietveld refinement of FePd$_3$ ($Pm\bar{3}m$) based on NPD (Figure 2) and XRPD data (Figure A1) using FullProf [24].

	Phase1	**Phase2 (Magnetic Phase)**	**Phase3**
contribution to pattern [1]	pattern 1 NPD pattern 2 NPD	pattern 1 NPD pattern 2 NPD	pattern 1 XRPD pattern 2 XRPD
a	$a1$	$a1$	$a3$
So(Fe)	*SOF*(Fe)	*SOF*(Fe)	*SOF*(Fe)
$B_{iso}(1a)$	$B_{iso}1(1a)$	$B_{iso}1(1a)$	$B_{iso}3(1a)$
$B_{iso}(3c)$	$B_{iso}1(3c)$	$B_{iso}1(3c)$	$B_{iso}3(3c)$

[1] Scale factors of patterns 1 and 2 of NPD and XRPD data are constrained, respectively; the profile parameters of each pattern are refined separately.

Table A6. Conditions and refined parameters of the Rietveld refinement of FePd$_3$ ($Pm\bar{3}m$) based on *in situ* NPD data (see Figures 2–4 and A9–A14, and Table A7) using FullProf [24].

| p/MPa	T/K	a/pm	$V/10^6$ pm^3	$B_{iso}(1a)/10^{-4}$ pm^2	$B_{iso}(3c)/10^{-4}$ pm^2	SOF(Fe, 1a) $_{1,2}$	SOF(D)
0.0001 (1)	296 (1)	385.204 (3)	57.157 (1)	2.17 (6)	1.11	0.875 (3)	$-^2$
0.50 (1)	296 (1)	385.217 (4)	57.163 (1)	2.03 (6)	1.19	0.847 (4)	0.013 (8)
1.00 (1)	296 (1)	385.230 (3)	57.169 (1)	1.80 (6)	1.27	0.847 (4)	0.015 (8)
2.00 (1)	296 (1)	385.254 (4)	57.180 (1)	1.69 (6)	1.28	0.844 (4)	0.017 (8)
4.00 (1)	296 (1)	385.290 (3)	57.196 (1)	2.00 (7)	1.13	0.834 (4)	0.027 (8)
8.00 (2)	296 (1)	385.372 (4)	57.232 (1)	2.15 (7)	1.05	0.794 (4)	0.047 (9)

[1] The stoichiometric ratio of Fe to Pd atoms was fixed at 1:3; [2] the Wyckoff position 1*b* is not occupied.

Table A7. Residual parameters of the Rietveld refinement of FePd$_3$ ($Pm\bar{3}m$) based on *in situ* NPD data (see Figures 2–4 and A9–A14, and Table A6) using FullProf [24].

p/MPa	R_{p1}	R_{p2}	R_{wp1}	R_{wp2}	χ^2	R_{Bragg1}	R_{Bragg2}
0.0001 (10)	0.057	0.069	0.080	0.087	2.38	2.15	7.03
0.50 (1)	0.058	0.073	0.084	0.090	2.49	2.59	15.1
1.00 (1)	0.057	0.068	0.080	0.086	2.42	2.32	11.0
2.00 (1)	0.057	0.065	0.079	0.083	2.37	2.14	10.3
4.00 (1)	0.056	0.064	0.077	0.081	2.32	1.97	13.2
8.00 (1)	0.058	0.062	0.077	0.081	2.52	2.74	18.3
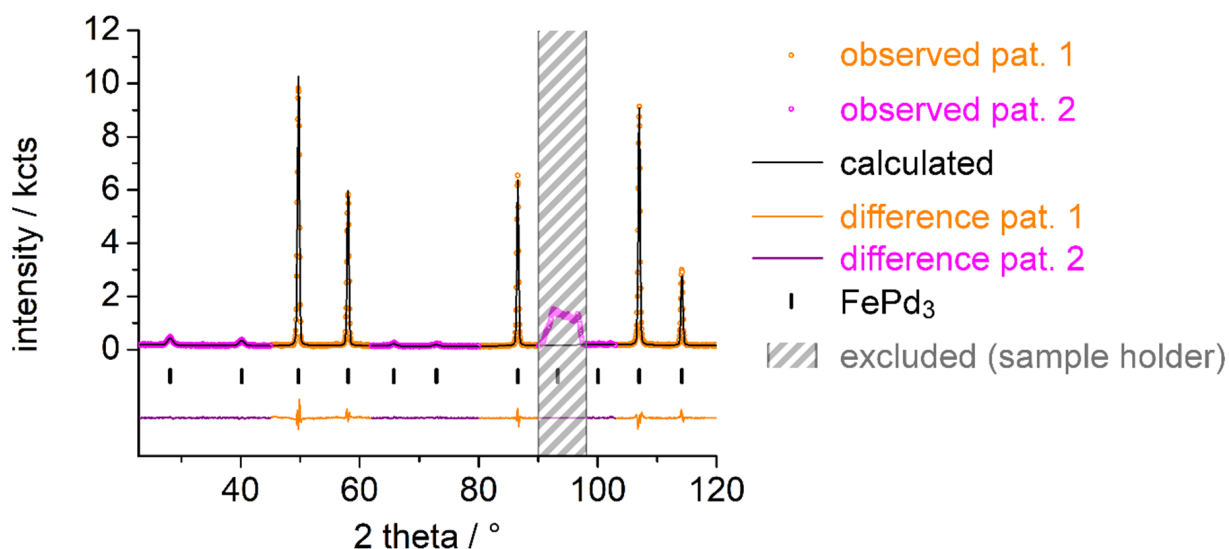
Figure A8. Rietveld refinement of the crystal structure of FePd$_3$ (for details, see first row in Tables A6 and A7) based on neutron powder diffraction data (NUMOR 131613 [21], λ = 186.80(2) pm, D20 ILL, Grenoble) in a single-crystal sapphire cell at 296(1) K and applied vacuum (0.0001(10) MPa) using FullProf [24].
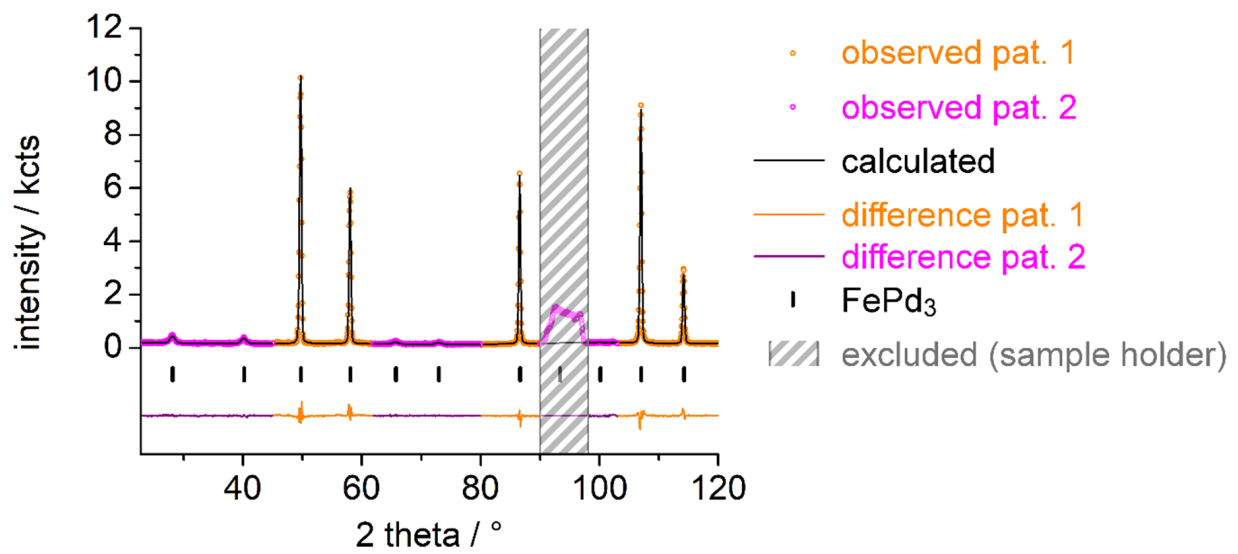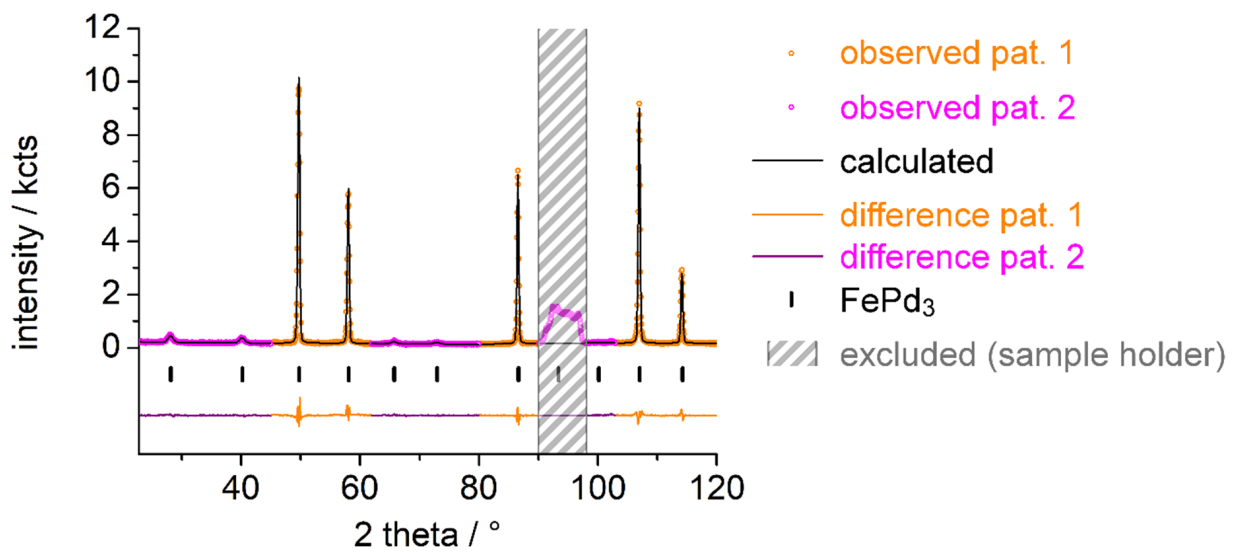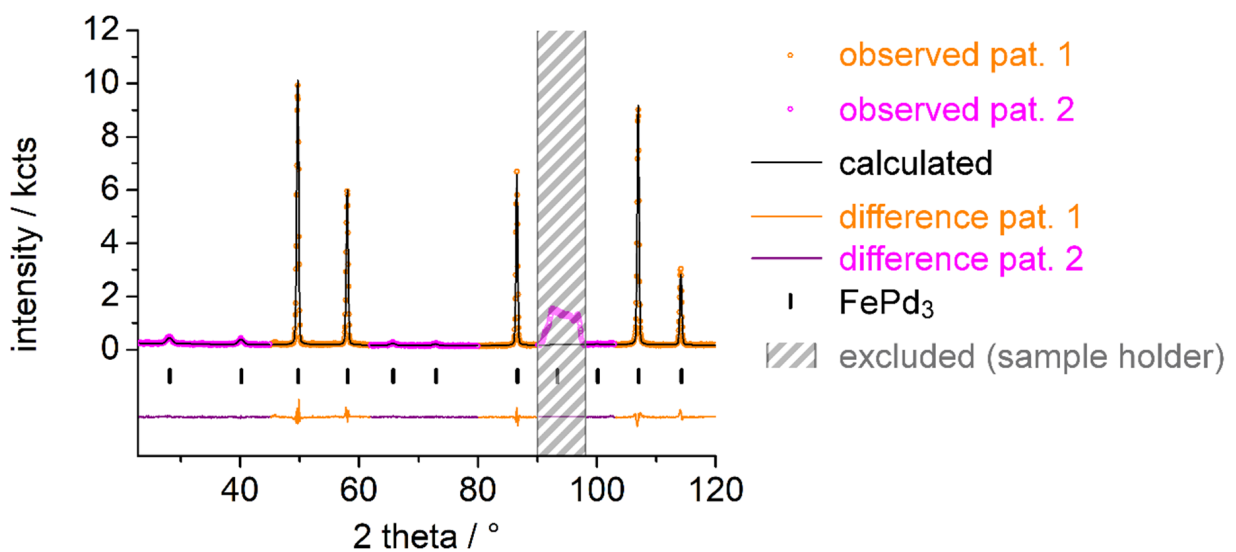
Figure A9. Rietveld refinement of the crystal structure of $FePd_3D_{0.013(8)}$ (for details, see second row in Tables A6 and A7) based on neutron powder diffraction data (NUMOR 131629 [21], λ = 186.80(2) pm, D20 ILL, Grenoble) in a single-crystal sapphire cell at 296(1) K and 0.50(1) MPa deuterium pressure using FullProf [24].
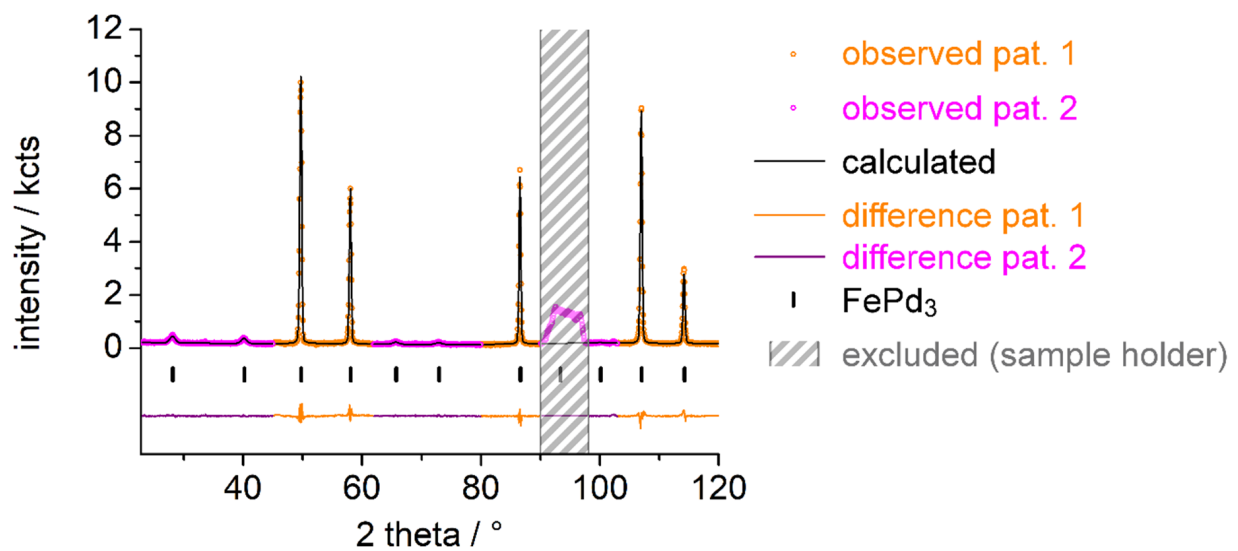
Figure A10. Rietveld refinement of the crystal structure of $FePd_3D_{0.015(8)}$ (for details, see third row in Tables A6 and A7) based on neutron powder diffraction data (NUMOR 131634 [21], λ = 186.80(2) pm, D20 ILL, Grenoble) in a single-crystal sapphire cell at 296(1) K and 1.00(1) MPa deuterium pressure using FullProf [24].
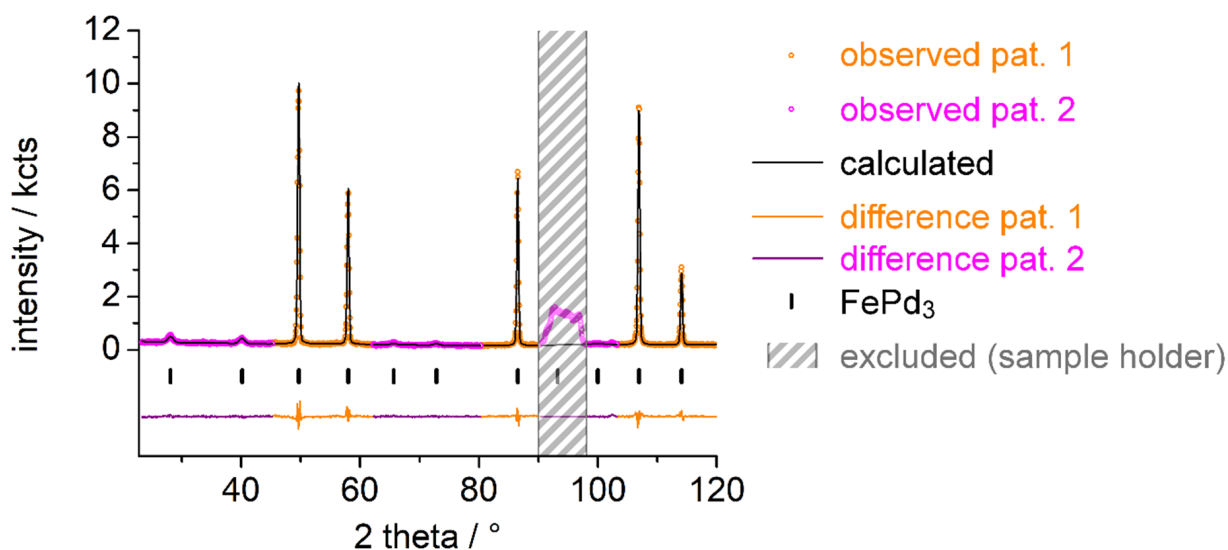
Figure A11. Rietveld refinement of the crystal structure of $FePd_3D_{0.017(8)}$ (for details, see fourth row in Tables A6 and A7) based on neutron powder diffraction data (NUMOR 131642 [21], λ = 186.80(2) pm, D20 ILL, Grenoble) in a single-crystal sapphire cell at 296(1) K and 2.00(1) MPa deuterium pressure using FullProf [24].

Figure A12. Rietveld refinement of the crystal structure of $FePd_3D_{0.027(8)}$ (for details, see fifth row in Tables A6 and A7) based on neutron powder diffraction data (NUMOR 131717 [21], λ = 186.80(2) pm, D20 ILL, Grenoble) in a single-crystal sapphire cell at 296(1) K and 4.00(1) MPa deuterium pressure using FullProf [24].

Figure A13. Rietveld refinement of the crystal structure of $FePd_3D_{0.047(9)}$ (for details, see sixth row in Tables A6 and A7, or first row in Tables A8 and A9) based on neutron powder diffraction data (NUMOR 131746 [21], λ = 186.80(2) pm, D20 ILL, Grenoble) in a single-crystal sapphire cell at 296(1) K and 8.00(1) MPa deuterium pressure using FullProf [24].

Table A8. Conditions and refined parameters of the Rietveld refinement of $FePd_3$ ($Pm\bar{3}m$) based on *in situ* NPD data (see Figures 2–4 and Table A9) using FullProf [24].

T/K	p/MPa	a/pm	V/10^6 pm^3	$B_{iso}(1a)$/10^{-4} pm^2	$B_{iso}(3c)$/10^{-4} pm^2	SOF(Fe, 1a) [1,2]	SOF(D)	R_z(Fe)/μ_B [1]
298 (1)	8.00 (1)	385.372 (4)	57.232 (1)	2.15 (7)	1.05	0.794 (3)	0.047 (9)	2.37 (11)
325 (3)	8.03 (1)	385.518 (4)	57.297 (1)	1.72 (6)	1.29	0.797 (4)	0.046 (9)	2.36 (12)
348 (3)	8.06 (1)	385.618 (3)	57.342 (1)	2.05 (7)	1.21	0.796 (4)	0.045 (9)	2.47 (11)
376 (3)	8.10 (1)	385.762 (4)	57.406 (1)	1.74 (7)	1.42	0.789 (4)	0.051 (9)	2.24 (12)
396 (3)	8.12 (1)	385.868 (4)	57.453 (1)	1.86 (7)	1.4	0.789 (4)	0.055 (9)	1.90 (13)
424 (3)	8.15 (1)	386.013 (4)	57.518 (1)	1.89 (7)	1.5	0.786 (4)	0.063 (9)	1.89 (14)
447 (3)	8.18 (1)	386.149 (4)	57.579 (1)	1.65 (8)	1.54	0.785 (4)	0.062 (10)	1.8 (2)
475 (3)	8.21 (1)	386.304 (4)	57.649 (1)	2.19 (8)	1.46	0.786 (4)	0.062 (10)	1.4 (2)
490 (3)	8.22 (1)	386.377 (4)	57.681 (1)	2.09 (8)	1.55	0.782 (4)	0.067 (10)	0.9 (3)
519 (2)	8.25 (1)	386.539 (4)	57.754 (1)	2.09 (9)	1.59	0.776 (4)	0.065 (11)	0.4 (7)
539 (1)	8.29 (1)	386.639 (4)	57.799 (1)	1.92 (9)	1.68	0.731 (4)	0.064 (10)	0 [3]
473 (2)	8.25 (1)	386.280 (4)	57.638 (1)	2.28 (9)	1.43	0.785 (4)	0.057 (9)	1.2 (2)
423 (2)	8.20 (1)	385.983 (4)	57.505 (1)	1.98 (7)	1.43	0.792 (3)	0.052 (9)	1.73 (13)
384 (1)	8.14 (1)	385.792 (3)	57.420 (1)	1.74 (6)	1.46	0.788 (3)	0.058 (9)	2.13 (12)
313 (1)	8.00 (1)	385.461 (4)	57.272 (1)	2.06 (7)	1.17	0.795 (4)	0.045(10)	2.39 (12)

[1] R_z was refined with fixed occupation from coupled refinement (Table 1); then, SOF was refined with fixed R_z; [2] The stoichiometric ratio of Fe to Pd atoms was fixed at 1:3; [3] R_z was fixed at 0.

Table A9. Residual parameters of the Rietveld refinement of $FePd_3$ ($Pm\bar{3}m$) based on *in situ* NPD data (see Figures 2–4 and Table A8) using FullProf [24].

T/K	R_{p1}	R_{p2}	R_{wp1}	R_{wp2}	χ^2	R_{Bragg1}	R_{Bragg2}	R_{Magn1}	R_{Magn2}
298 (1)	0.058	0.062	0.077	0.081	2.52	2.74	18.3	2.60	20.5
325 (3)	0.059	0.058	0.081	0.074	2.54	3.41	21.3	3.97	14.5
348 (3)	0.056	0.059	0.075	0.073	2.29	2.03	9.46	2.38	9.68
376 (3)	0.054	0.057	0.075	0.073	2.31	2.07	10.5	2.28	10.3
396 (3)	0.054	0.058	0.075	0.074	2.33	2.74	13.6	3.28	10.2
424 (3)	0.057	0.055	0.079	0.070	2.45	3.38	13.5	3.59	12.7
447 (3)	0.058	0.057	0.080	0.072	2.54	3.57	9.79	3.31	6.46

Table A9. *Cont.*

| *T*/K	R_{p1}	R_{p2}	R_{wp1}	R_{wp2}	χ^2	R_{Bragg1}	R_{Bragg2}	R_{Magn1}	R_{Magn2}
475 (3)	0.060	0.055	0.083	0.071	2.71	4.00	17.0	4.14	15.9
490 (3)	0.058	0.057	0.082	0.073	2.70	3.69	26.1	3.86	22.7
519 (2)	0.060	0.055	0.087	0.069	2.95	4.56	27.0	5.32	25.0
539 (1)	0.058	0.056	0.085	0.070	2.86	3.65	31.6	- [1]	- [1]
473 (2)	0.059	0.058	0.082	0.074	2.78	4.38	36.9	4.51	24.7
423 (2)	0.057	0.055	0.079	0.070	2.42	3.38	28.0	3.73	12.7
384 (1)	0.053	0.059	0.073	0.074	2.24	2.44	9.15	2.55	10.3
313 (1)	0.062	0.062	0.085	0.078	2.79	3.16	31.5	3.98	15.1

[1] R_z was fixed at 0.
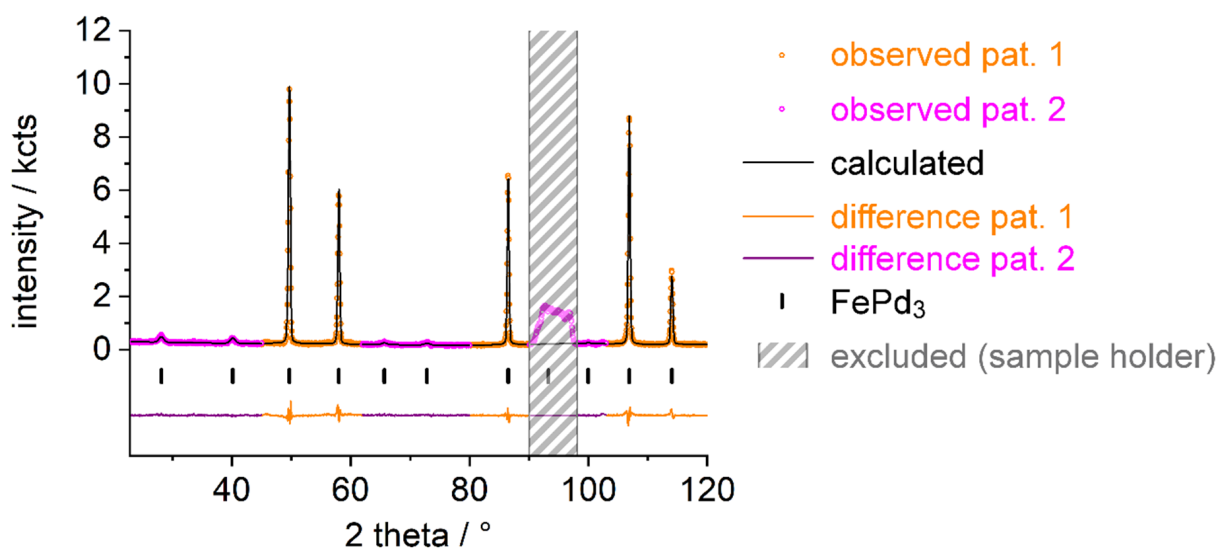
Figure A14. Rietveld refinement of the crystal structure of $FePd_3D_{0.046(9)}$ (for details, see second row in Tables A8 and A9) based on neutron powder diffraction data (NUMOR 131755 [21], λ = 186.80(2) pm, D20 ILL, Grenoble) in a single-crystal sapphire cell at 325(3) K and 8.03(1) MPa deuterium pressure using FullProf [24].
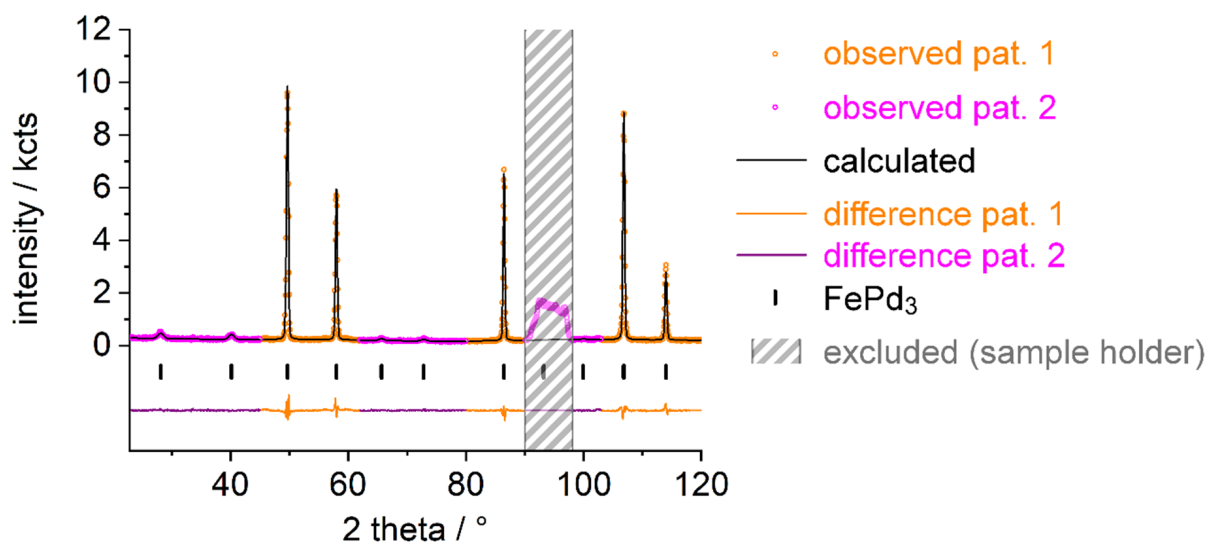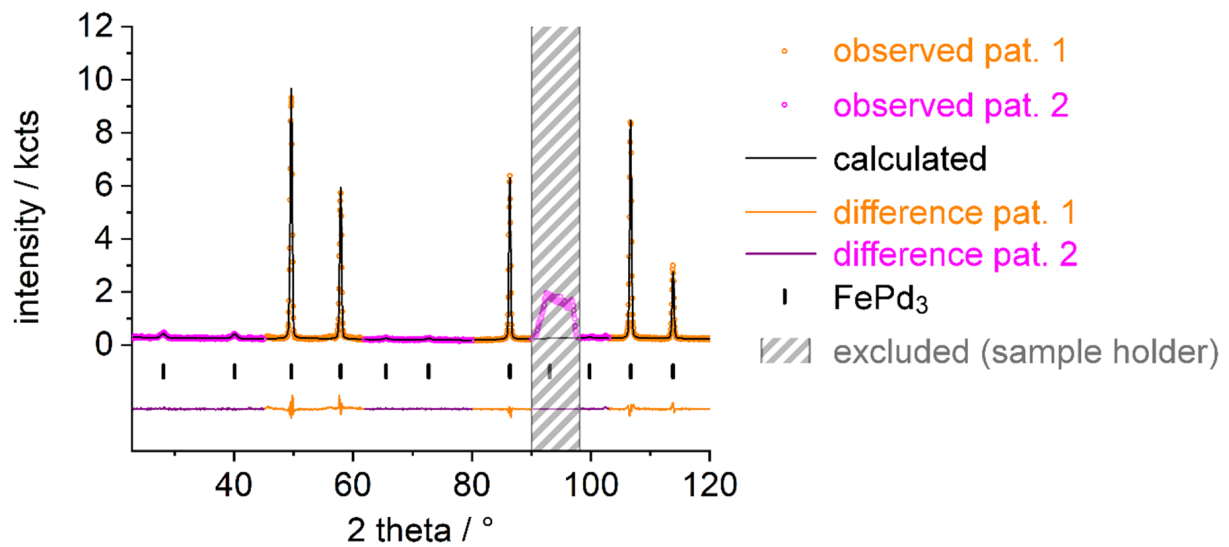

Figure A15. Rietveld refinement of the crystal structure of $FePd_3D_{0.045(9)}$ (for details, see third row in Tables A8 and A9) based on neutron powder diffraction data (NUMOR 131760 [21], λ = 186.80(2) pm, D20 ILL, Grenoble) in a single-crystal sapphire cell at 348(3) K and 8.06(1) MPa deuterium pressure using FullProf [24].
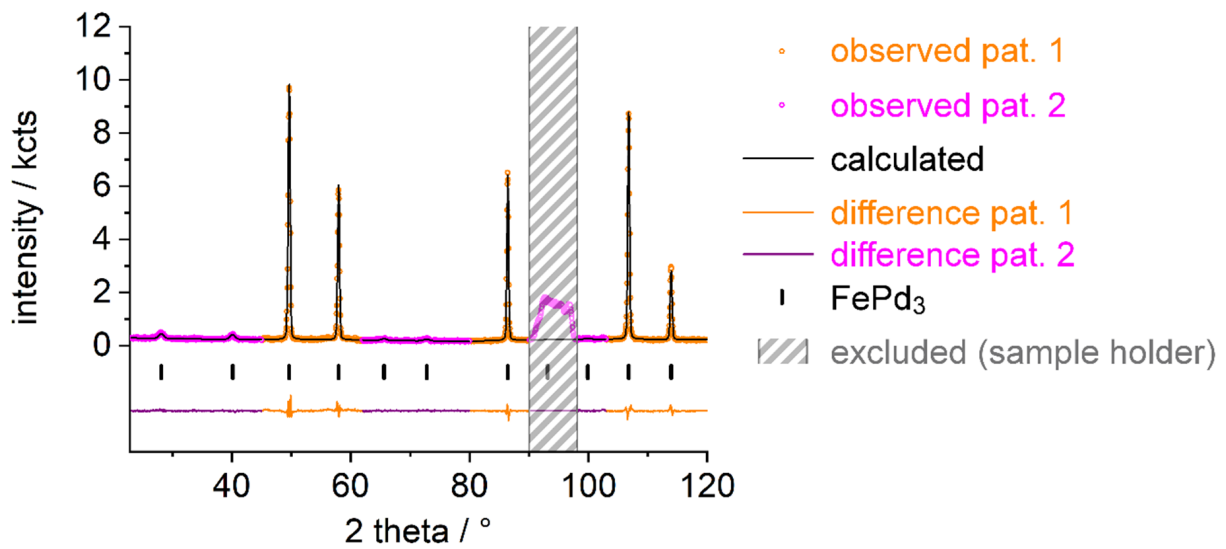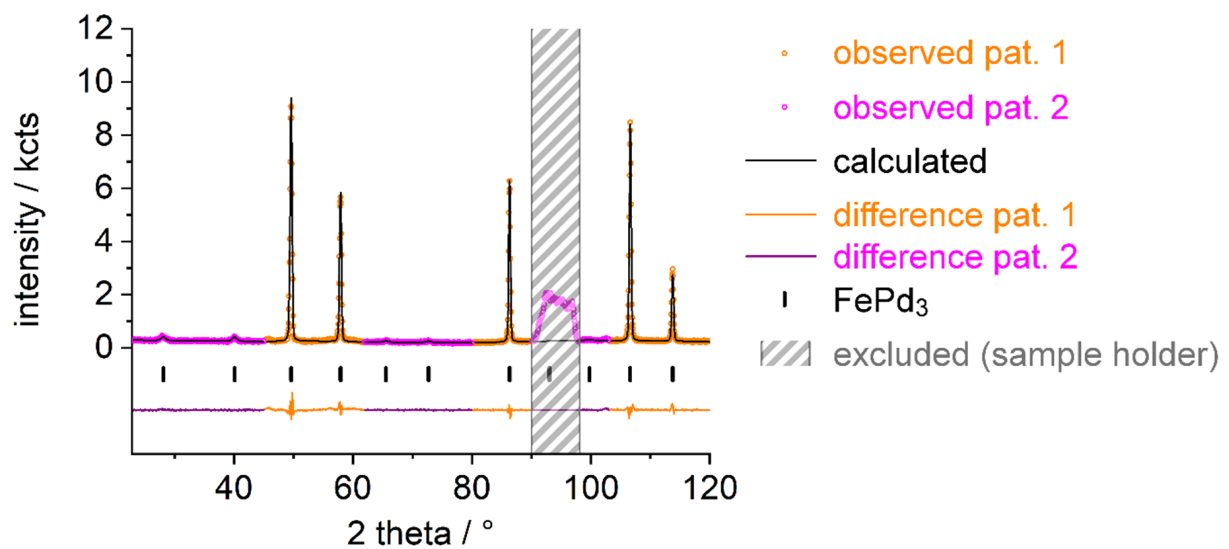
Figure A16. Rietveld refinement of the crystal structure of $FePd_3D_{0.051(9)}$ (for details, see fourth row in Tables A8 and A9) based on neutron powder diffraction data (NUMOR 131765 [21], $\lambda = 186.80(2)$ pm, D20 ILL, Grenoble) in a single-crystal sapphire cell at 376(3) K and 8.10(1) MPa deuterium pressure using FullProf [24].
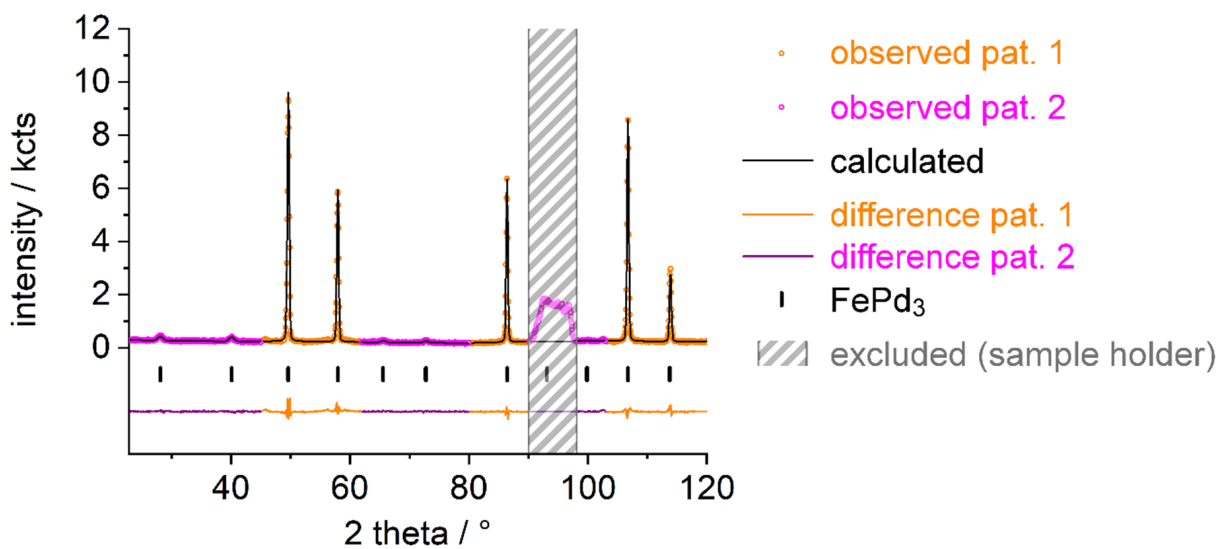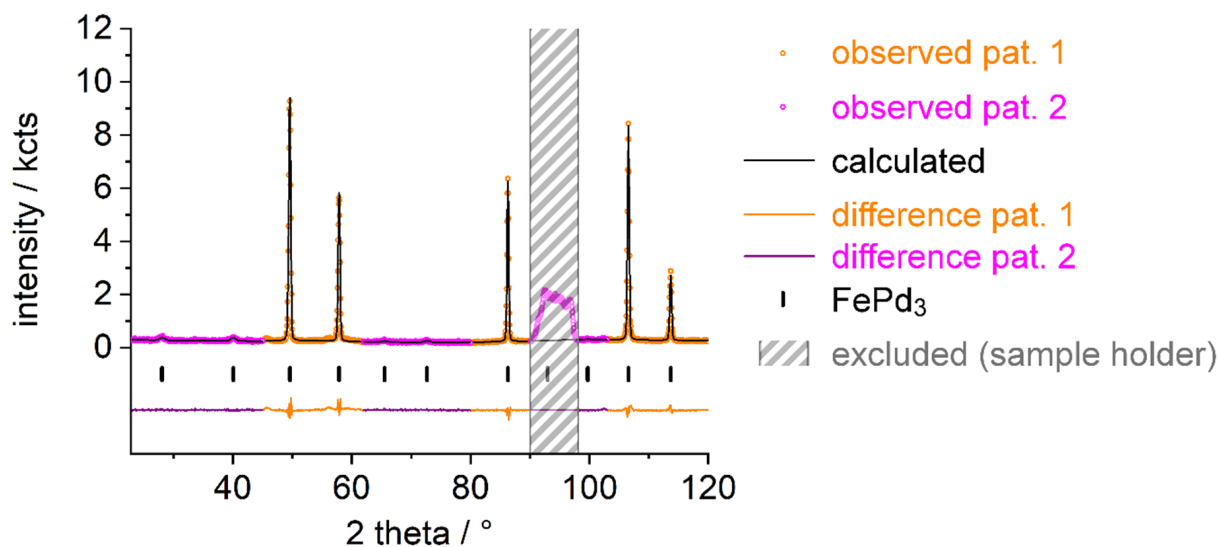

Figure A17. Rietveld refinement of the crystal structure of $FePd_3D_{0.055(9)}$ (for details, see fifth row in Tables A8 and A9) based on neutron powder diffraction data (NUMOR 131768 [21], $\lambda = 186.80(2)$ pm, D20 ILL, Grenoble) in a single-crystal sapphire cell at 396(3) K and 8.12(1) MPa deuterium pressure using FullProf [24].
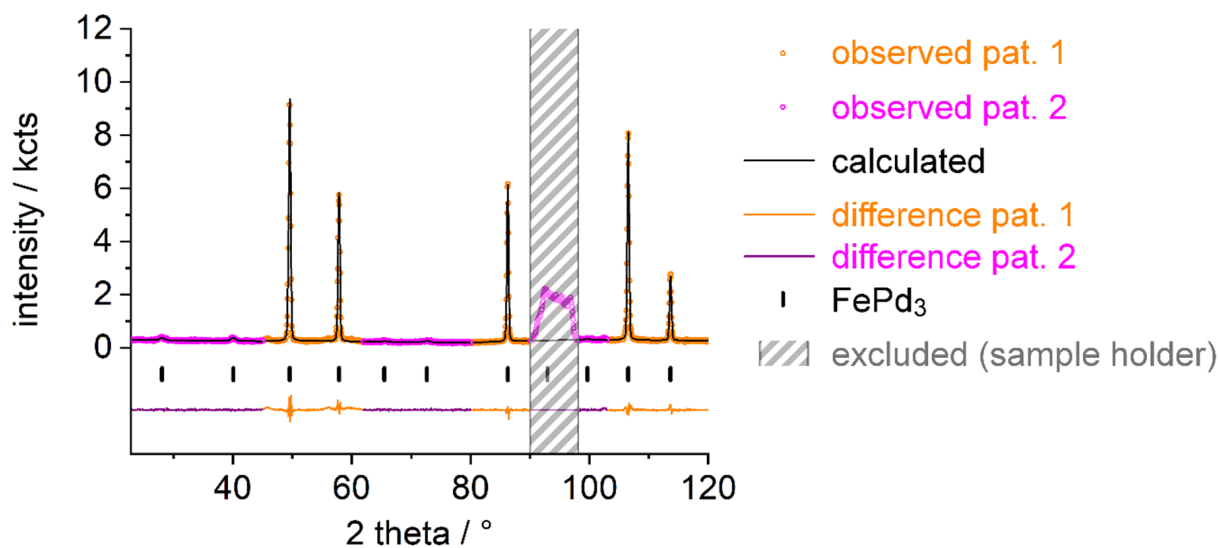
Figure A18. Rietveld refinement of the crystal structure of $FePd_3D_{0.063(9)}$ (for details, see sixth row in Tables A8 and A9) based on neutron powder diffraction data (NUMOR 131772 [21], λ = 186.80(2) pm, D20 ILL, Grenoble) in a single-crystal sapphire cell at 424(3) K and 8.15(1) MPa deuterium pressure using FullProf [24].

Figure A19. Rietveld refinement of the crystal structure of $FePd_3D_{0.062(10)}$ (for details, see seventh row in Tables A8 and A9) based on neutron powder diffraction data (NUMOR 131776 [21], λ = 186.80(2) pm, D20 ILL, Grenoble) in a single-crystal sapphire cell at 447(3) K and 8.18(1) MPa deuterium pressure using FullProf [24].
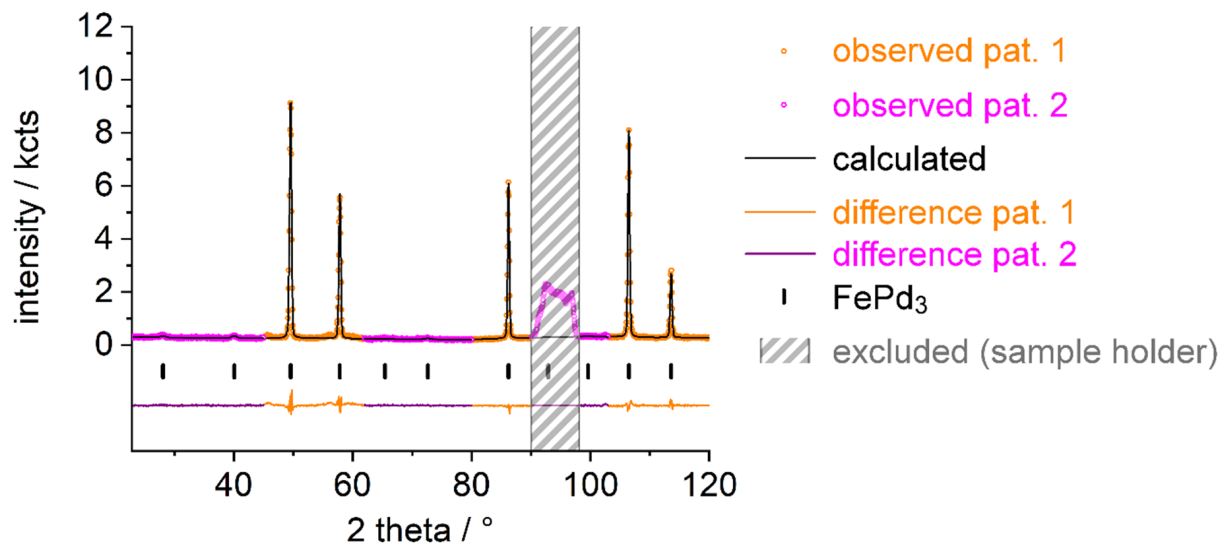
Figure A20. Rietveld refinement of the crystal structure of $FePd_3D_{0.062(10)}$ (for details, see eighth row in Tables A8 and A9) based on neutron powder diffraction data (NUMOR 131781 [21], λ = 186.80(2) pm, D20 ILL, Grenoble) in a single-crystal sapphire cell at 475(3) K and 8.21(1) MPa deuterium pressure using FullProf [24].
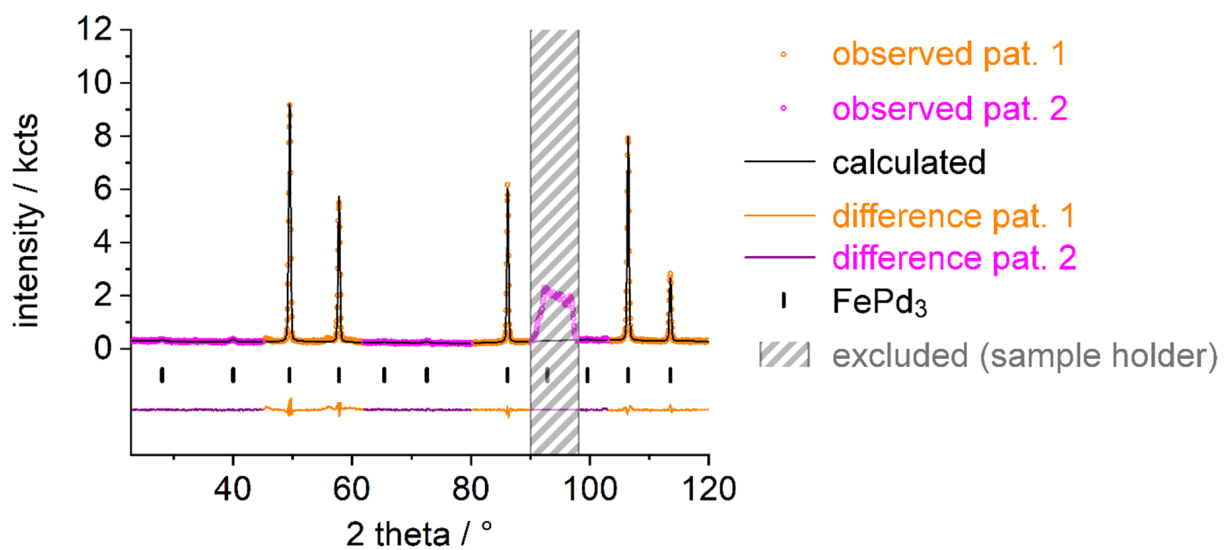

Figure A21. Rietveld refinement of the crystal structure of $FePd_3D_{0.067(10)}$ (for details, see ninth row in Tables A8 and A9) based on neutron powder diffraction data (NUMOR 131783 [21], λ = 186.80(2) pm, D20 ILL, Grenoble) in a single-crystal sapphire cell at 490(3) K and 8.22(1) MPa deuterium pressure using FullProf [24].

Figure A22. Rietveld refinement of the crystal structure of $FePd_3D_{0.065(11)}$ (for details, see tenth row in Tables A8 and A9) based on neutron powder diffraction data (NUMOR 131791 [21], λ = 186.80(2) pm, D20 ILL, Grenoble) in a single-crystal sapphire cell at 519(2) K and 8.25(1) MPa deuterium pressure using FullProf [24].
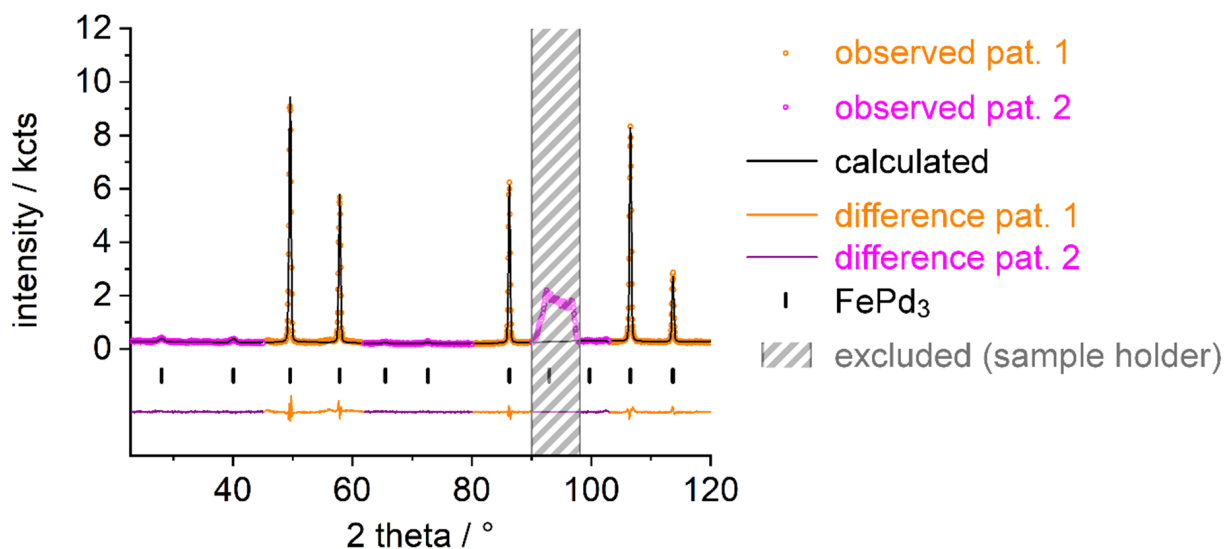

Figure A23. Rietveld refinement of the crystal structure of $FePd_3D_{0.064(10)}$ (for details, see eleventh row in Tables A8 and A9) based on neutron powder diffraction data (NUMOR 131815 [21], λ = 186.80(2) pm, D20 ILL, Grenoble) in a single-crystal sapphire cell at 539(1) K and 8.29(1) MPa deuterium pressure using FullProf [24].

Figure A24. Rietveld refinement of the crystal structure of $FePd_3D_{0.057(9)}$ (for details, see twelfth row in Tables A8 and A9) based on neutron powder diffraction data (NUMOR 131833 [21], $\lambda = 186.80(2)$ pm, D20 ILL, Grenoble) in a single-crystal sapphire cell at 473(2) K and 8.25(1) MPa deuterium pressure using FullProf [24].
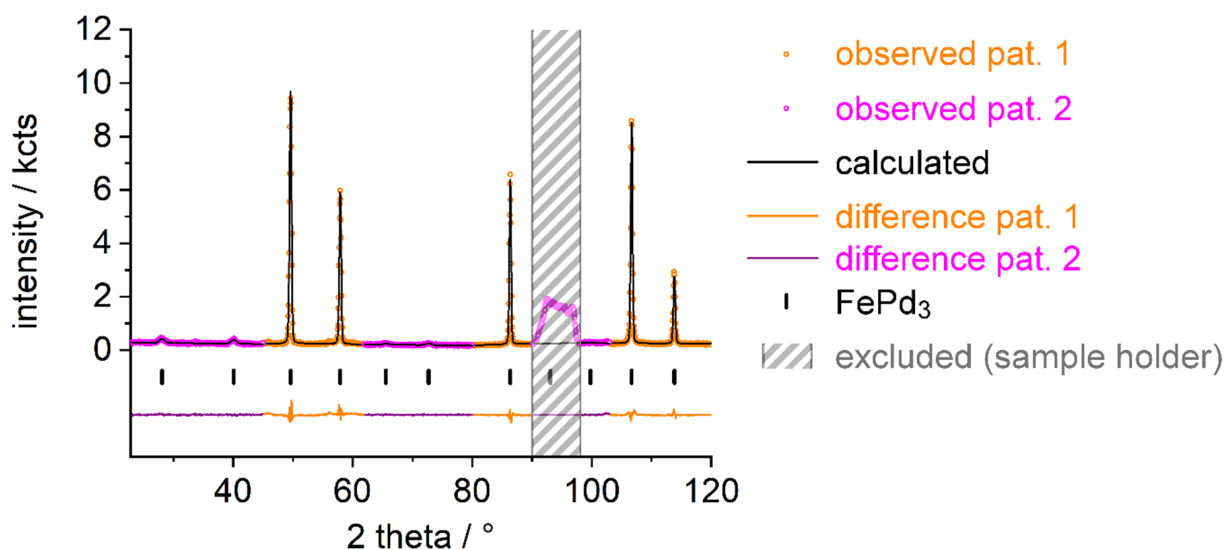

Figure A25. Rietveld refinement of the crystal structure of $FePd_3D_{0.052(9)}$ (for details, see thirteenth row in Tables A8 and A9) based on neutron powder diffraction data (NUMOR 131847 [21], $\lambda = 186.80(2)$ pm, D20 ILL, Grenoble) in a single-crystal sapphire cell at 423(2) K and 8.20(1) MPa deuterium pressure using FullProf [24].
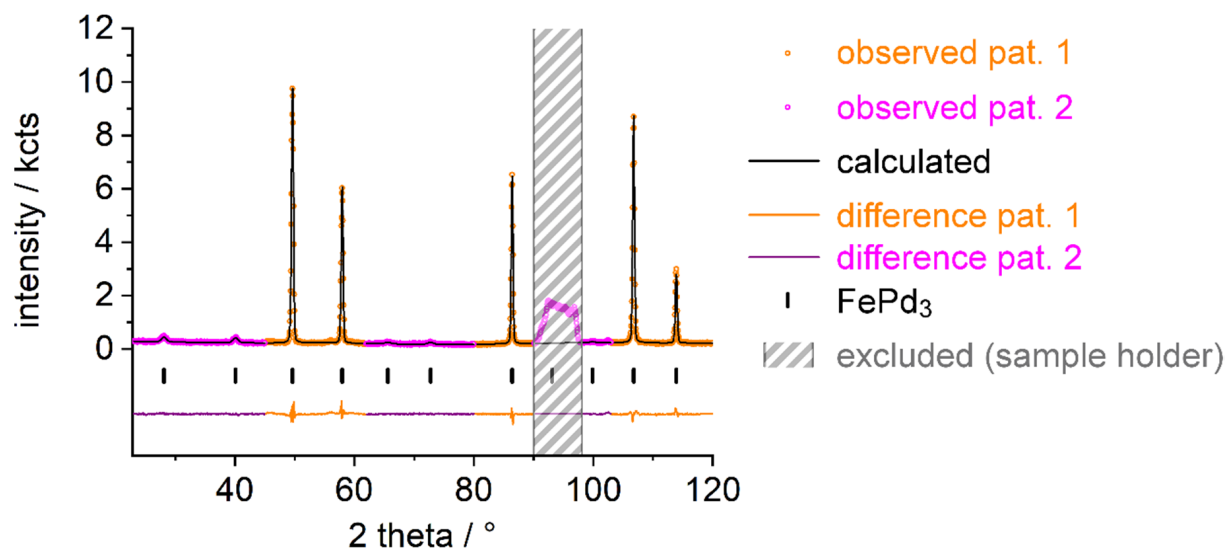
Figure A26. Rietveld refinement of the crystal structure of $FePd_3D_{0.058(9)}$ (for details, see fourteenth row in Tables A8 and A9) based on neutron powder diffraction data (NUMOR 131859 [21], $\lambda = 186.80(2)$ pm, D20 ILL, Grenoble) in a single-crystal sapphire cell at 384(1) K and 8.14(1) MPa deuterium pressure using FullProf [24].
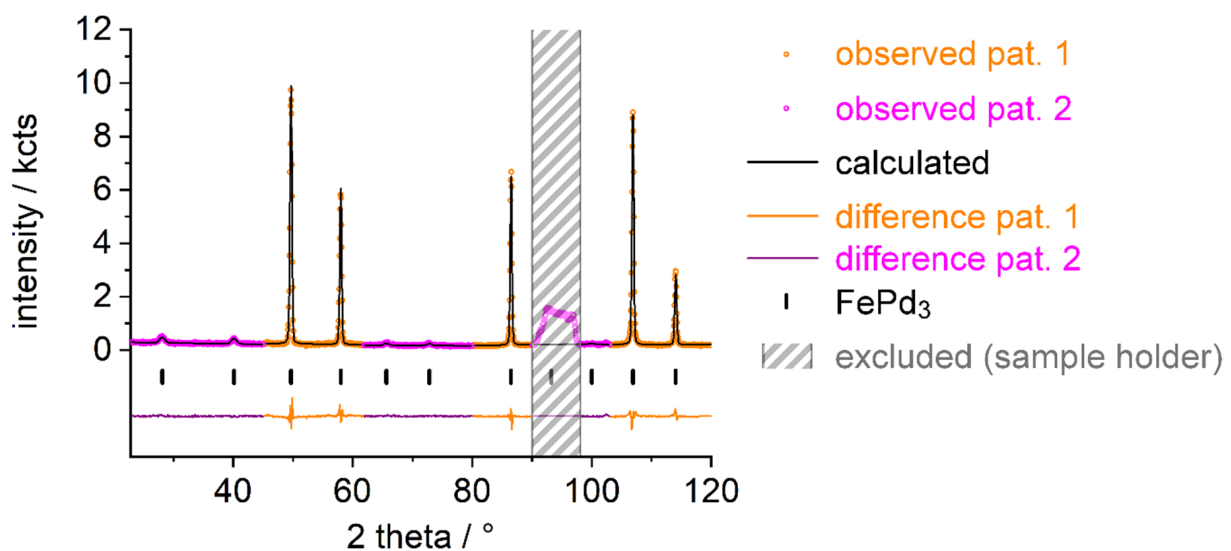

Figure A27. Rietveld refinement of the crystal structure of $FePd_3D_{0.045(10)}$ (for details, see fifteenth row in Tables A8 and A9) based on neutron powder diffraction data (NUMOR 131894 [21], $\lambda = 186.80(2)$ pm, D20 ILL, Grenoble) in a single-crystal sapphire cell at 313(1) K and 8.00(1) MPa deuterium pressure using FullProf [24].

References

1. Buschow, K.H.J.; Bouten, P.C.P.; Miedema, A.R. Hydrides formed from intermetallic compounds of two transition metals: A special class of ternary alloys. *Rep. Prog. Phys.* **1982**, *45*, 937–1039. [CrossRef]
2. Aoki, K.; Masumoto, T. Hydrogen-induced amorphization of intermetallics. *J. Alloys Compd.* **1995**, *231*, 20–28. [CrossRef]
3. Kvashnin, Y.O.; Khmelevskyi, S.; Kudrnovský, J.; Yaresko, A.N.; Genovese, L.; Bruno, P. Noncollinear magnetic ordering in compressed FePd3 ordered alloy: A first principles study. *Phys. Rev. B* **2012**, *86*, 174429. [CrossRef]
4. Winterrose, M.L.; Lucas, M.S.; Yue, A.F.; Halevy, I.; Mauger, L.; Muñoz, J.A.; Hu, J.; Lerche, M.; Fultz, B. Pressure-induced invar behavior in Pd3Fe. *Phys. Rev. Lett.* **2009**, *102*, 237202. [CrossRef]
5. Ridley, C.J.; Bull, C.L.; Funnell, N.P.; Capelli, S.C.; Manuel, P.; Khalyavin, D.D.; O'Neill, C.D.; Kamenev, K.V. High-pressure neutron diffraction study of Pd3Fe. *J. Appl. Phys.* **2019**, *125*, 15901. [CrossRef]

6. Longworth, G. Temperature dependence of the Fe^{57} hfs in the ordered alloys FePd$_3$ and FePd near the Curie temperature. *Phys. Rev.* **1968**, *172*, 572–576. [CrossRef]

7. Guo, J.; Ye, Q.; Lan, M.; Wang, S.; Yu, T.; Gao, F.; Hu, D.; Wang, P.; He, Y.; Boi, F.S.; et al. Cl-assisted highly efficient synthesis of FePd$_3$ alloys encapsulated in graphite papers: A two stage CVD approach. *RSC Adv.* **2016**, *6*, 40676–40682. [CrossRef]

8. Boi, F.S.; Guo, J.; Lan, M.; Xiang, G.; He, Y.; Wang, S.; Chen, H. *In Situ* encapsulation of Pd crystals inside foam-like carbon films continuously filled with α-Fe: Investigating the nucleation of FePd$_3$ alloys. *RSC Adv.* **2016**, *6*, 54189–54192. [CrossRef]

9. Boi, F.S.; Du, Y.; Ivaturi, S.; He, Y.; Wang, S. New insights on the magnetic properties of ferromagnetic FePd$_3$ single-crystals encapsulated inside carbon nanomaterials. *Mater. Res. Express* **2017**, *4*, 35021. [CrossRef]

10. Cui, Z.; Li, L.; Manthiram, A.; Goodenough, J.B. Enhanced cycling stability of hybrid Li–air batteries enabled by ordered Pd$_3$Fe intermetallic electrocatalyst. *J. Am. Chem. Soc.* **2015**, *137*, 7278–7281. [CrossRef]

11. Liu, Z.; Fu, G.; Li, J.; Liu, Z.; Xu, L.; Sun, D.; Tang, Y. Facile synthesis based on novel carbon-supported cyanogel of structurally ordered Pd$_3$Fe/C as electrocatalyst for formic acid oxidation. *Nano Res.* **2018**, *11*, 4686–4696. [CrossRef]

12. Dimas-Rivera, G.L.; La Rivera De Rosa, J.; Lucio-Ortiz, C.J.; Martínez-Vargas, D.X.; Sandoval-Rangel, L.; García Gutiérrez, D.I.; Solis Maldonado, C. Bimetallic Pd-Fe supported on γ-Al$_2$O$_3$ catalyst used in the ring opening of 2-methylfuran to selective formation of alcohols. *Appl. Catal. A* **2017**, *543*, 133–140. [CrossRef]

13. Yu, W.; Porosoff, M.D.; Chen, J.G. Review of Pt-based bimetallic catalysis: From model surfaces to supported catalysts. *Chem. Rev.* **2012**, *112*, 5780–5817. [CrossRef] [PubMed]

14. Yang, J.; Li, S.; Zhang, L.; Liu, X.; Wang, J.; Pan, X.; Li, N.; Wang, A.; Cong, Y.; Wang, X.; et al. Hydrodeoxygenation of furans over Pd-FeO$_x$/SiO$_2$ catalyst under atmospheric pressure. *Appl. Catal. B* **2017**, *201*, 266–277. [CrossRef]

15. von Goldbeck, O.K. *Iron—Binary Phase Diagrams*; Springer Berlin Heidelberg: Berlin/Heidelberg, Germany, 1982; pp. 88–91. [CrossRef]

16. Konovalova, E.V.; Perevalova, O.B.; Koneva, N.A.; Veselov, S.V.; Kozlov, E.V. Effect of ordering kinetics on the degree of far atomic order in Pd$_3$Fe alloy. *Bull. Russ. Acad. Sci. Phys.* **2013**, *77*, 288–291. [CrossRef]

17. Flanagan, T.B.; Majchrzak, S.; Baranowski, B. A chemical reaction strongly dependent upon the degree of order of an alloy: The absorption of hydrogen by Pd$_3$Fe. *Philos. Mag.* **1972**, *25*, 257–262. [CrossRef]

18. Lewis, F.A. The Palladium-Hydrogen System, Part III: Alloy Systems and Hydrogen Permeation. *Platin. Met. Rev.* **1982**, *26*, 121–128.

19. Finger, R.; Kurtzemann, N.; Hansen, T.C.; Kohlmann, H. Design and use of a sapphire single-crystal gas-pressure cell for *in situ* neutron powder diffraction. *J. Appl. Crystallogr.* **2021**, *54*, 839–846. [CrossRef] [PubMed]

20. Götze, A.; Auer, H.; Finger, R.; Hansen, T.C.; Kohlmann, H. A sapphire single-crystal cell for *in situ* neutron powder diffraction of solid-gas reactions. *Physica B* **2018**, *551*, 395–400. [CrossRef]

21. Kohlmann, H.; Finger, R.; Götze, A.; Hansen, T.C.; Pflug, C.; Werwein, A. *Reaction Pathways of Hydrogenation-Dehydrogenation of InPd$_3$ and FePd$_3$ by In Situ Neutron Diffraction*; Institut Laue-Langevin: Grenoble, France, 2018. [CrossRef]

22. Rietveld, H.M. Line profiles of neutron powder-diffraction peaks for structure refinement. *Acta Crystallogr.* **1967**, *22*, 151–152. [CrossRef]

23. Rietveld, H.M. A profile refinement method for nuclear and magnetic structures. *J. Appl. Crystallogr.* **1969**, *2*, 65–71. [CrossRef]

24. Rodríguez-Carvajal, J. *FullProf*; Institut Laue-Langevin: Grenoble, France, 2012.

25. *TOPAS*; Bruker AXS GmbH: Karlsruhe, Germany, 2014.

26. Önnerud, P.; Andersson, Y.; Tellgren, R.; Nordblad, P. The Magnetic Structure of Ordered Cubic Pd$_3$Mn. *J. Solid State Chem.* **1997**, *128*, 109–114. [CrossRef]

27. Worsham, J.E., Jr.; Wilkinson, M.K.; Shull, C.G. Neutron-diffraction observations on the palladium-hydrogen and palladium-deuterium systems. *J. Phys. Chem. Solids* **1957**, *3*, 303–310. [CrossRef]

28. Pickart, S.J.; Nathans, R. Alloys of the first transition series with Pd and Pt. *J. Appl. Phys.* **1962**, *33*, 1336–1338. [CrossRef]

29. Delley, B.; Jarlborg, T.; Freeman, A.J.; Ellis, D.E. All-electron local density theory of local magnetic moments in metals. *J. Magn. Magn. Mater.* **1983**, *31–34*, 549–550. [CrossRef]

30. Pathak, R.; Kashyap, A. Boron interstitials in ordered phases of Fe-Pd binary alloys: A first principle study. *J. Magn. Magn. Mater.* **2021**, *528*, 167766. [CrossRef]

31. Götze, A.; Urban, P.; Oeckler, O.; Kohlmann, H. Synthesis and Crystal Structure of Pd$_5$InSe. *Z. Nat. B Chem. Sci.* **2014**, *69*, 417–422. [CrossRef]

32. Wannek, C.; Harbrecht, B. Iodine-promoted synthesis of structurally ordered AlPd$_5$. *Z. Anorg. Allg. Chem.* **2007**, *633*, 1397–1402. [CrossRef]

33. Mohn, P.; Supanetz, E.; Schwarz, K. Electronic structure and spin fluctuations in the fcc Fe-Pd system. *Aust. J. Phys.* **1993**, *46*, 651. [CrossRef]

34. Kaul, S.N. Static critical phenomena in ferromagnets with quenched disorder. *J. Magn. Magn. Mater.* **1985**, *53*, 5–53. [CrossRef]

35. Ahlzén, P.-J.; Andersson, Y.; Tellgren, R.; Rodic, D.; Flanagan, T.B.; Sakamoto, Y. A Neutron Powder Diffraction Study of Pd$_3$MnD$_x$. *Z. Phys. Chem.* **1989**, *163*, 213–218. [CrossRef]

36. Sieverts, A.F. Absorption of gases by metals. *Z. Met.* **1929**, *21*, 37–46.

37. Önnerud, P.; Andersson, Y.; Tellgren, R.; Nordblad, P.; Bourée, F.; André, G. The crystal and magnetic structures of ordered cubic Pd$_3$MnD$_{0.7}$. *Solid State Commun.* **1997**, *101*, 433–437. [CrossRef]

38. Kohlmann, H.; Skripov, A.V.; Soloninin, A.V.; Udovic, T.J. The anti-perovskite type hydride InPd$_3$H$_{0.89}$. *J. Solid State Chem.* **2010**, *183*, 2461–2465. [CrossRef]

39. Götze, A.; Kohlmann, H. *Palladium Hydride and Hydrides of Palladium-Rich Phases. Reference Module in Chemistry, Molecular Sciences and Chemical Engineering*; Elsevier: Amsterdam, The Netherlands, 2017.

40. Jaswal, S.S. Electronic structure and magnetism in VPd$_3$ and FePd$_3$. *Phys. Rev. B* **1982**, *53*, 8213–8214. [CrossRef]

41. Kuhnen, C.A.; da Silva, E.Z. Electronic structure of Pd$_3$Fe: Ordered phase. *Phys. Rev. B* **1987**, *35*, 370–376. [CrossRef] [PubMed]

42. Wu, D.-H.; Wang, H.-C.; Wei, L.-T.; Pan, R.-K.; Tang, B.-Y. First-principles study of structural stability and elastic properties of MgPd$_3$ and its hydride. *J. Magnes. Alloys* **2014**, *2*, 165–174. [CrossRef]

43. Jaswal, S.S. Electronic structure and magnetism in transition metal compounds: VNi$_3$, MnPd$_3$ and MoPd$_3$. *Solid State Commun.* **1984**, *52*, 127–129. [CrossRef]

44. Nautiyal, T.; Auluck, S. The electronic structure and magnetism of MoPd$_3$ and MnPd$_3$. *Phys. Rev. B* **1989**, *1*, 2211–2215. [CrossRef]

45. Mousa, A.A.; Jaradat, R.; Abu-Jafar, M.; Mahmoud, N.T.; Al-Qaisi, S.; Khalifeh, J.M.; Abusaimeh, H. Theoretical investigation of the structural, electronic, and elastic properties of *TM*$_3$In (*TM* = Pd and Pt) intermetallic compounds. *AIP Adv.* **2020**, *10*, 65317. [CrossRef]

46. Kunkel, N.; Sander, J.; Louis, N.; Pang, Y.; Dejon, L.M.; Wagener, F.; Zang, Y.N.; Sayede, A.; Bauer, M.; Springborg, M.; et al. Theoretical investigation of the hydrogenation induced atomic rearrangements in palladium rich intermetallic compounds MPd$_3$ (M=Mg, In, Tl). *Eur. Phys. J. B* **2011**, *82*, 1–6. [CrossRef]

47. Marker, V.; Wolf, G.; Baranowski, B. Effect of long-range order and hydrogen content on the low-temperature heat capacity of Pd$_3$Fe. *Phys. Status Solidi A* **1974**, *26*, 167–173. [CrossRef]

48. Jung, C.G. *Collected Works of C.G. Jung, Volume 9 (Part 1): Archetypes and the Collective Unconscious*; Princeton University Press: Princeton, NJ, USA, 1969.